Journal of Nanobiotechnology

RESEARCH

Open Access

Regulation of immune microenvironments by polyetheretherketone surface topography for improving osseointegration

Yuqing Zhao[1†], Yanxin An[2†], Fan Wu[1], Lipeng Liu[3], Franklin R. Tay[4], Yang Jiao[5*] and Jing Wang[1*]

Abstract

Optimizing the immune microenvironment is essential for successful implant osseointegration. In this study, four different nano/microstructures were fabricated on polyetheretherketone (PEEK) substrates by varying the agitation speed during sulfonation to influence osteoimmunomodulation and implant integration. The results indicate that nano/microstructures with minimal dimensions (SP450) inhibit actin polymerization by reducing calcium influx through PIEZO1, activating the anti-inflammatory M2 macrophage phenotype. Among the tested specimens, SP450 exhibited the lowest expression levels of tumor necrosis factor-α and interleukin-1β while releasing the highest levels of anti-inflammatory factors, including interleukin-4 and interleukin-10. This optimized immune environment promotes the osteogenesis of MC3T3-E1 pre-osteoblasts and enhances the osseointegration of PEEK implants. Transcriptomic analysis and validation experiment further revealed that SP450 inhibits osteoclastic differentiation by down-regulating transforming growth factor-β2 and suppressing the NF-κB signaling pathway. These findings suggest that manipulating the surface topography of PEEK implants is an effective strategy for enhancing osseointegration with promising clinical applications.

Keywords Macrophage polarization, Nano/microstructures, Osteoimmunomodulation, Osseointegration, Polyetheretherketone

†Yuqing Zhao and Yanxin An contributed equally to this work.

*Correspondence:
Yang Jiao
jiaoyang1989731@163.com
Jing Wang
jingwang@fmmu.edu.cn
[1]State Key Laboratory of Oral & Maxillofacial Reconstruction and Regeneration, National Clinical Research Center for Oral Diseases, Shaanxi Engineering Research Center for Dental Materials and Advanced Manufacture, Department of Oral Implants, School of Stomatology, The Fourth Military Medical University, Xi'an 710032, PR China
[2]Department of General Surgery, The First Affiliated Hospital of Xi'an Medical University, Xi'an 710077, PR China
[3]State Key Laboratory of Oral & Maxillofacial Reconstruction and Regeneration, National Clinical Research Center for Oral Diseases, Shaanxi Clinical Research Center for Oral Diseases, Department of Pediatric Dentistry, School of Stomatology, The Fourth Military Medical University, Xi'an 710032, PR China
[4]The Graduate School, Augusta University, Augusta, GA 30912, USA
[5]Department of Stomatology, The Seventh Medical Center of PLA General Hospital, Beijing 100700, PR China

Introduction

Polyetheretherketone (PEEK) has received increasing interest as an alternative to metal in orthopedics and dental implantology. This is attributed to its excellent mechanical properties, low cytotoxicity, thermal/chemical stability, and natural radiolucency. The polymer has been approved by The US Food and Drug Administration for use in the human body [1, 2]. As a thermoplastic polymer, PEEK may be processed through three-dimensional (3D) printing technology to manufacture customized implants with complex structures to meet the requirements of personalized and precise repair [3, 4]. Because the modulus of elasticity of PEEK is comparable to that of cortical bone (3–4 GPa), this alleviates implant loosening caused by stress shielding (a biomechanical phenomenon causing adaptive changes in bone strength and stiffness around metallic implants) and reduces peri-implant bone resorption [5, 6]. However, the inherent biological inertia and poor osteoinductivity of PEEK severely impede its integration with native bone tissues. Formation of fibrous wrapping around implants fabricated from PEEK results in expedited implant failure [7].

Modifications have been conducted recently to improve the osteogenic activity of PEEK. Commonly used surface modification methods include deposition techniques (incorporating bioactive particles or metal coating onto the PEEK surface) and modification of surface topography (sulfonation, plasma treatment, and laser treatment) [8, 9]. Nevertheless, these methods are associated with problems such as poor coating stability, complicated fabrication process, and high cost. Sulfonation is a simple and effective modification method that can quickly form porous structures and provide a rough surface for loading bioactive molecules or further treatment [10, 11]. Zhao et al. first reported the fabrication of a 3D porous network on the surface of PEEK using sulfonation. The sulfonated PEEK exhibited improved bioactivity, biocompatibility, osseointegration, and bone-implant bond strength [12]. Ouyang et al. further demonstrated that hydrothermal treatment enhanced both osseointegration and antibacterial resistance of sulfonated PEEK [13]. The authors previously fabricated an irregular porous monolayer on the surface of PEEK by sulfonation and nitrification. The osteogenic activity of the monolayer structure was similar to that of a 3D porous network in vitro, while its osseointegration potential was significantly improved in vivo [14].

Osteoimmunology refers to the study of the interface between the skeletal system and the immune system. A favorable osteoimmunological environment is required to facilitate bone regeneration and repair. After implant placement, the bone-implant interface is rapidly filled with a fibrin coagulum enriched with growth factors and cytokines. The coagulum contains platelets, erythrocytes, neutrophils, macrophages (MΦ), and debris of cortical and trabecular bone [15]. Among the cellular components, MΦs play a central role in the early stage of bone remodeling. Activated MΦs proliferate and switch into two major subtypes coined M1 and M2, respectively. Specifically, the recruited MΦs that reach the implant surface are activated into the M1 phenotype. This is followed by the secretion of tumor necrosis factor (TNF)-α, interleukin (IL)-1β, IL-6, and IL-12 to promote pathogen killing and activation of inflammation [16, 17]. The M1 phenotype typically stays at the injury site for 3–4 days after injury. After that, the phenotype changes to M2. The M2-phenotypic MΦs release anti-inflammatory cytokines, including IL-4, IL-10, and transforming growth factor (TGF)-β [18, 19]. These signals from the local environment benefit vascularization and bone regeneration. Nevertheless, prolonged or unrestrained retention of M1 MΦs may cause damage to the surrounding cells or tissues due to their excessive production of pro-inflammatory cytokines. The latter is detrimental to biomaterial-mediated tissue repair and regeneration and may ultimately cause failure of implants [20, 21]. Hence, timely switching of MΦs from the M1 to the M2 phenotype during tissue repair is highly conducive to osseointegration and bone regeneration.

The polarization capability of MΦs is sensitive to the physicochemical properties of biomaterials. Surface properties (e.g., surface charge, chirality, wettability, and stiffness) and surface topography (e.g., surface roughness, 2D topography, and 3D geometry) have been implicated in the biological response of MΦs when they are approaching or in contact with biomaterials [22, 23]. Previous studies showed that RAW 264.7 MΦs cultured in vitro on rough surfaces were activated to the M2 phenotype compared to those cultured on polished surfaces. This finding suggests that nanomaterials with rough surfaces have the potential to promote wound repair and bone regeneration [24, 25]. The authors previously reported that TiO_2 nanotubes with a diameter of 70 nm, among all length scales investigated, could induce the differentiation of RAW 264.7 MΦs to the pro-healing M2 phenotype. Nanotubules of that dimension augmented the osteogenic potential of mesenchymal stem cells and the angiogenic ability of human umbilical vein endothelial cells *via* multiple paracrine signaling [26]. To date, the underlying mechanism of how surface topographical cues regulate MΦ behaviors and the immune microenvironment is unknown.

In this study, a series of nano/microstructures with different dimensions were fabricated on PEEK substrates by controlling the agitation speeds of sulfonation (Fig. 1). Morphology change, polarization, and inflammatory response of MΦs on different nano/microstructures were systematically examined. MC3T3-E1 pre-osteoblasts

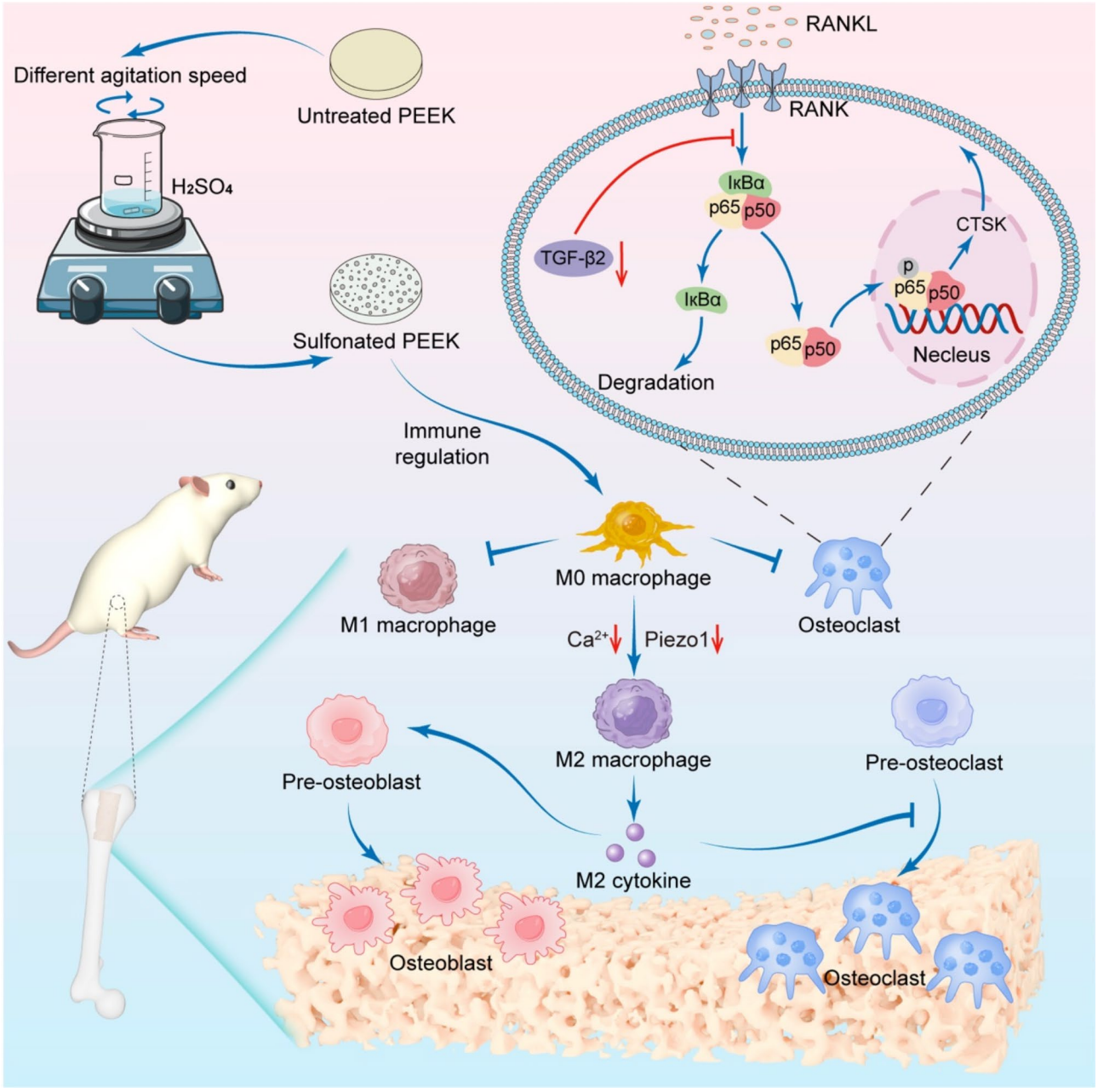

Fig. 1 Schematic illustration of this study. The "lotus-type" topography on PEEK was fabricated within a short time by controlling the agitation speed of sulfonation. The minimal dimension (SP450) showed greater potential in reducing calcium influx through PIEZO1 to modulate nonactivated macrophage polarization to an anti-inflammatory M2 phenotype, inducing the secretion of anti-inflammatory cytokines, and suppressing osteoclastic differentiation of macrophages through the inhibition of NF-κB signaling pathway by down-regulating TGF-β2. The favorable local immune environment eventually facilitates new bone formation and osseointegration

were cultured directly with different PEEK nano/microstructures or with MΦ supernatant collected after exposure to PEEK nano/microstructures in vitro. The osteogenic differentiation potential of the cultured pre-osteoblasts was then evaluated. In vivo experiments were performed to verify the osseointegration capacity of functionalized implants. Finally, transcriptomic analysis and validation experiments were used to elucidate the potential mechanisms by which PEEK surface topography influences immunomodulation.

Results and discussion

Surface characterization of PEEK specimens

Sulfonation is a one-step manufacturing method for surface modification of PEEK-based implants. Previous studies have demonstrated that the porous structure

gradually became more evident and complicated with increased sulfonation time [27, 28]. However, the surface morphology was found to be different with the same sulfonation time across studies [27, 29, 30]. In the present study, it was found that the surface topography of PEEK was related to the agitation speed of magnetic stirring. Accordingly, the sulfonation time was set as 30 s, and the four experimental groups were named SP450, SP550, SP650, and SP750 based on different agitation speeds (450 rpm, 550 rpm, 650 rpm, and 750 rpm), respectively. Figure 2a represents field emission-scanning electron microscopy (FE-SEM) images of the surface topography of the PEEK specimens. The polished PEEK surface was relatively smooth, while the surface of SP450 and SP550 showed "lotus-type" topography. The nano/microstructures changed from monolayer to multilayer with an increase in agitation speed. The surfaces of SP650 and SP750 showed a 3D porous network structure with several layers of interconnecting pores. The average pore sizes of the experimental groups SP450, SP550, SP650, and SP750 were 239.37 ± 17.52 nm, 594.11 ± 35.71 nm, 1322.38 ± 123.71 nm, and 1566.97 ± 126.35 nm, respectively (Fig. 2c).

Sulfonation of PEEK depends on the collision of PEEK and concentrated sulfuric acid [12]. Achieving a high reaction rate from two immiscible reactants is challenging due to the limited contact area [31]. As agitation speeds increase, the contact surface area between the two

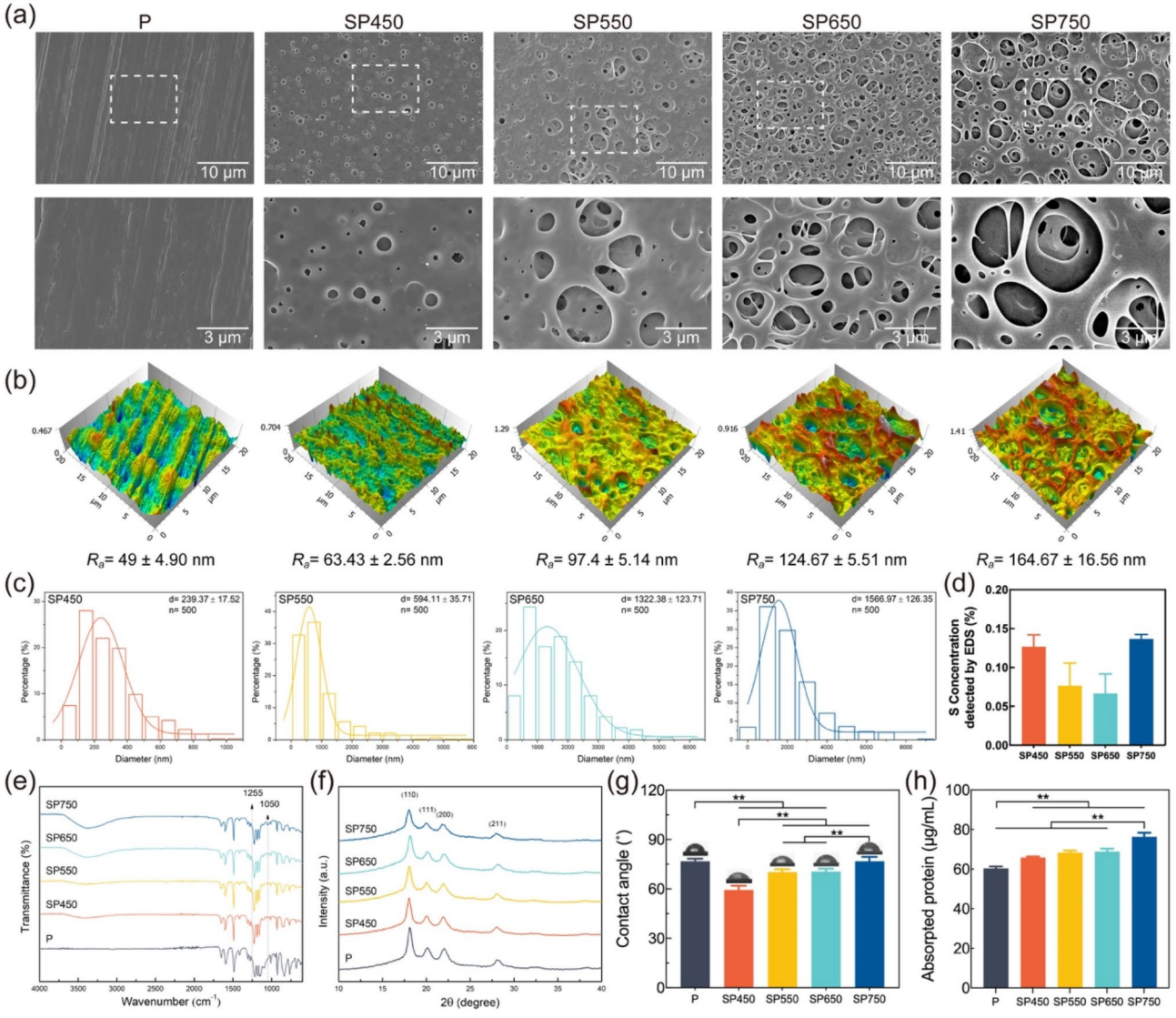

Fig. 2 Surface characterizations of PEEK specimens. (**a**) Surface morphology of different specimens examined with SEM. (**b**) Surface roughness of the specimens examined by AFM. (**c**) Diameter distribution of different specimens. (**d**) Sulfur (S) concentration examined with EDS. (**e**) FTIR spectra of different specimens. (**f**) XRD spectra of different specimens. a.u., arbitrary units. (**g**) Contact angles of water on different specimens. (**h**) Amount of adsorbed fibronectin on different specimens. $n = 3$ independent experiments per group; $^{**}P < 0.01$

phases improves, resulting in various topographies on PEEK. The topographical features of the PEEK specimens were further analyzed by atomic force microscopy (AFM) (Fig. 2b). Consistent with the SEM results, the roughness of the sulfonated layer roughness increased with agitation speed. Compared with the control P group, there were a lot of pores on the surface of SP450. However, the roughness of SP450, measuring approximately 50 nm, closely resembled that of the P group. Given that the surface roughness of bone is about 32 nm, the nano/microstructure of SP450 most closely approximated the natural roughness of bone, making it an excellent mimic [32].

Energy dispersive spectroscopy (EDS) indicated that the sulfur content of the sulfonated specimens was all lower than 0.15% after ultrasonic cleaning with acetone and hydrothermal treatment (Fig. 2d). Ouyang et al. reported that minimal sulfur release enhances cell proliferation and antibacterial ability [13]. Infrared spectra of the PEEK specimens, collected with the use of Fourier transform-infrared spectroscopy (FT-IR) (Fig. 2e), revealed a broad band at ~3200–3500 cm^{-1} that was ascribed to the OH vibrational peak of -SO_3H. Additional characteristic bands, such as the S = O symmetric stretching vibration peak at 1050 cm^{-1} and the O = S = O asymmetric stretching vibration peak at 1255 cm^{-1}, indicated the presence of -SO_3H in the specimens derived from the four experimental groups. These results indicated that the residual H_2SO_4 could be removed via ultrasonic cleaning and hydrothermal treatment, but the covalently bonded -SO_3H groups on PEEK substrates were well retained. X-ray diffraction (XRD) (Fig. 2f) showed that the characteristic PEEK peaks decreased after sulfonation; those peaks were further reduced upon increased agitation speed. These results indicated that the introduction of -SO_3H disrupted the macromolecular arrangement of the PEEK polymer, resulting in a decrease in crystallinity and the formation of a porous structure.

Contact angles made by water on the surfaces of PEEK specimens are summarized in Fig. 2g. Compared with P, the contact angles of SP450, SP550, and SP650 significantly decreased. The increase in hydrophilicity was attributed to the incorporation of increasing numbers of the hydrophilic -SO_3H functional group. A previous study reported that the nanostructures on titanium increased hydrophilicity through the capillary effect [33]. The number of nanopores in the experimental groups decreased with increased agitation speed, which may account for the increased contact angle. According to the FT-IR results, -SO_3H was also incorporated into SP750. However, there was no difference in the contact angle between P and SP750. These results were consistent with the study of Wang et al., which suggested that a water drop on the roughened surface might interact with a heterogeneous surface composed of the solid material and air trapped in the micro/nano-topography. This interaction increases the contact angle on the porous heterogeneous specimens of the SP750 group [27]. Fibronectin, a major non-collagenous glycoprotein in the extracellular matrix, is of interest due to its role in mediating cell-surface interaction [34]. Thus, the amount of fibronectin adsorption on different specimens was examined (Fig. 2h). Compared with P, the amount of fibronectin adsorption on SP450, SP550, SP650, and SP750 significantly increased. This increase may be attributed to the larger pore size.

Sterilization is the final surface treatment procedure of all implants, and also is one of the key factors that must be considered before implementation. As a practical and cost-effective sterilization option, autoclave treatment is widely used to sterilize medical and surgical devices. Previous studies demonstrated that autoclave sterilization could detrimentally affect the TiO_2 nanoporous structures [35, 36]. This phenomenon may attribute to the boiling and repeated expansion of water molecules entrapped within the nanostructures; These processes exert significant mechanical stress on the nanopore walls, consequently undermining the structural integrity of the walls [37]. In present study, the topography of PEEK specimens remained unaltered after autoclave sterilization at 103.4 kPa, 121.3 °C for a duration of 30 min. On one hand, the temperature employed in autoclave sterilization is lower than the glass transition temperature of PEEK [38]. On the other hand, when contrasted with TiO_2 nanotubes assembled layer-by-layer on the surface of titanium *via* hydrothermal treatment or electrochemical anodization, the nano/micro-pores formed by sulfonation on PEEK exhibit greater stability. The fact that autoclaving has no discernible impact on PEEK topography holds great promise for the future clinical translation of sulfonated PEEK.

Biocompatibility of PEEK specimens

To study the in vitro biocompatibility of specimens, MΦ and MC3T3-E1 pre-osteoblasts were seeded on each group of PEEK specimens, respectively. Cell adhesion is a critical process for subsequent cell proliferation and functioning on biomaterials [39]. Based on the fluorescence staining results shown in Fig. 3a-b, the number of MΦ nuclei for all groups increased with time (1–4 h). There was little difference in the number of adherent MΦ between 2-h and 4-h incubation. This observation suggests that the MΦs completed their adhesion process after 2 h of incubation. At all time points, the number of MC3T3-E1 pre-osteoblasts that adhered to the surface of sulfonated specimens was significantly higher than those that adhered to the smooth PEEK, which was the same as that of MΦs (Figure S1a-b). In addition, the quantity of

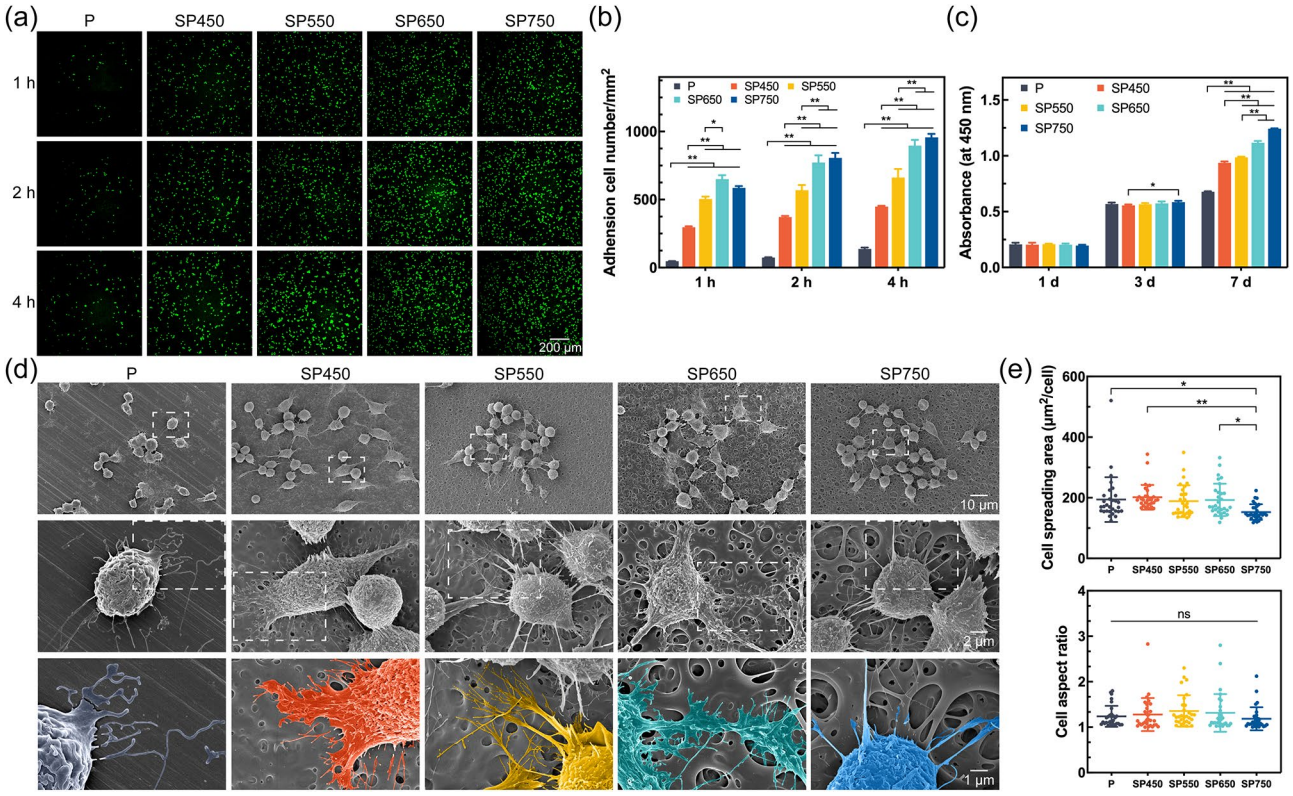

Fig. 3 In vitro Raw 264.7 MΦs behaviors on various nanostructures. (**a**) Adherent MΦs that adhered to different PEEK specimens at 1 h, 2 h, and 4 h. Cell nuclei were stained with DAPI; Scale bars: 200 μm. (**b**) Histogram of MΦs population that adhered to the PEEK specimens. (**c**) CCK-8 assay results of the proliferation of MΦs after 1 d, 3 d, and 7 d of culture on PEEK specimens with different dimensions. (**d**) SEM of the MΦs morphology on different specimens. (**e**) Quantitative cell spreading area and cell aspect ratio based on SEM images. $n = 3$ independent experiments *per* group; $^{*}P < 0.05$ and $^{**}P < 0.01$

MΦ adhesion increased with the pore size of the nano/microstructures [40].

Live/dead staining and CCK-8 assays were performed to assess cell viability. With increasing culture time, almost no dead cells (stained red) were observed on any of the surfaces at any time point (Figure S1c). Regarding cell proliferation, Figure S1d shows a higher rate of metabolic activity of osteoblasts on sulfonated PEEK at day 3, which was significantly enhanced at day 7. Cell absorbance values increased as the cell culture time of MΦs increased from 1 to 7 days (Fig. 3c). The sulfonated PEEK specimens were more adept at promoting MΦ proliferation than the smooth PEEK specimens after 7 days of culture. Moreover, MΦ proliferation on the sulfonated specimens increased with pore size. These results suggested that all the specimens supported osteoblast and MΦ growth with no perceptible cytotoxicity.

Low-magnification SEM images showed that all five specimens promoted osteoblast adhesion and spreading (Figure S1e). Osteoblasts cultured on sulfonated PEEK showed extended and flat lamellipodia compared to the control P group. As mentioned previously, the increased hydrophilicity can facilitate extracellular matrix protein adhesion to varying degrees, providing numerous spacing sites for clusters of adhered integrin to promote cell spreading [41]. The strong adhesion of actin filaments, which creates a network of elongated fibers on the sulfonated PEEK, is expected to facilitate osteogenesis.

Figure 3d shows the morphology of MΦs after 3 days of culture. The MΦs were sparsely distributed over the P specimens. In contrast, the MΦs grew in clusters on the sulfonated specimens. The MΦs that grew on top of SP450, SP550, and SP650 specimens exhibited an irregular shape with cytoplasm spread out, whereas those that grew on P and SP750 specimens bulged up and appeared spherical. High magnification images of the MΦs on the sulfonated PEEK specimens revealed abundant filopodia, many of which had penetrated the pores of the nano/microstructures. In contrast, the MΦs present on the P specimens only developed a few filopodia that contacted the smooth PEEK surface. In addition, more particulate matter could be seen on the surface of MΦs on the sulfonated specimens. These results demonstrated that PEEK nano/microstructures may influence MΦ spreading and secretion. Quantitative analyses of cell spreading area and cell aspect ratio based on SEM images (Figure S2) are shown in Fig. 3e. The MΦs present on SP750 had a lower spreading area than the other four groups. This

observation suggests that excessive pore size restricted cell spreading and filopodia formation. There was no significant difference in cell aspect ratio among different groups.

Effects of the specimen surface characteristics on inflammatory responses of MΦs

Activated MΦs switch polarization states in response to topographic cues derived from nanomaterials present in the wound microenvironment [42, 43]. Hence, the effects of PEEK nano/microstructures on MΦ polarization were further investigated (Fig. 4a). Inducible nitric

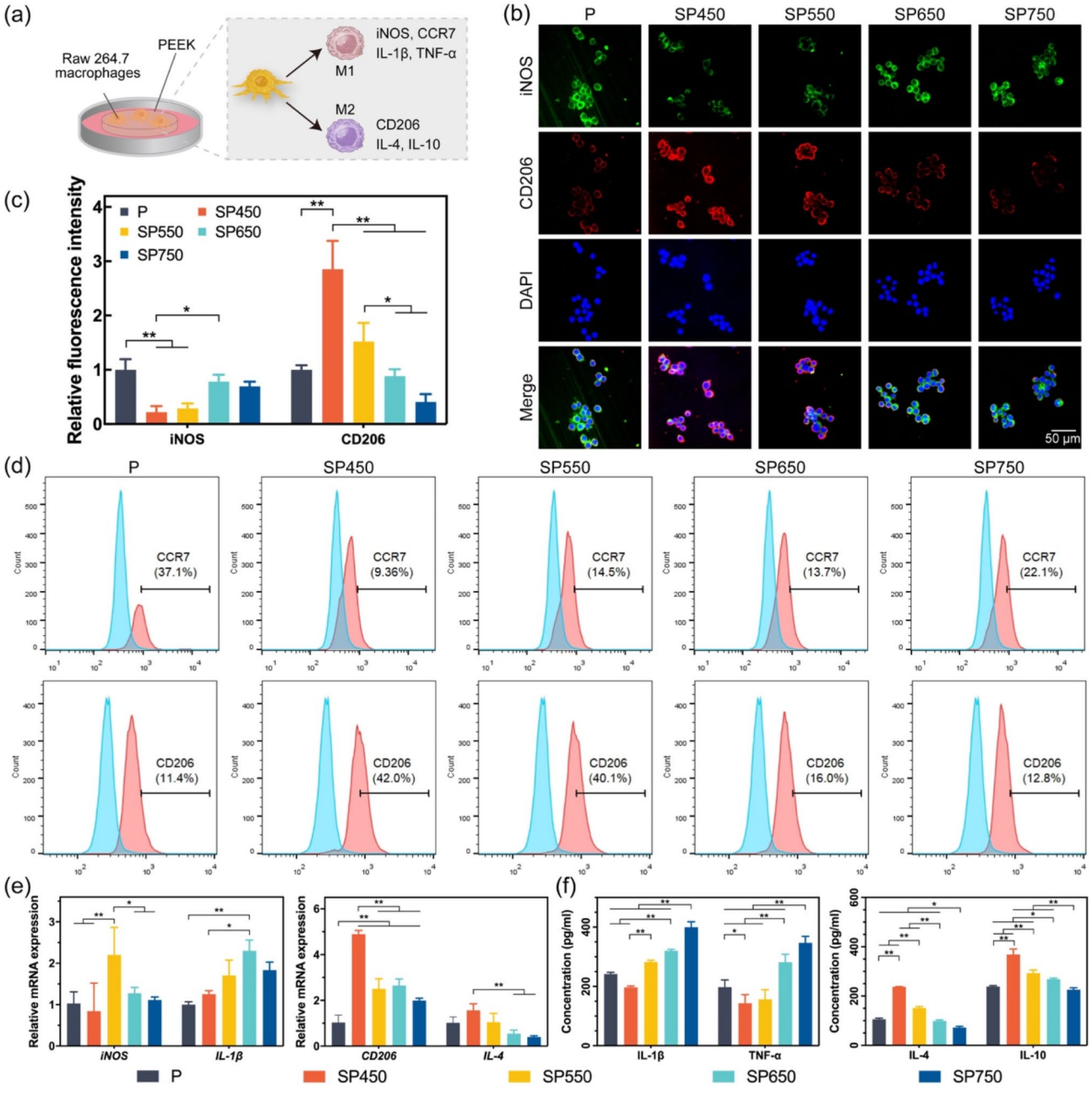

Fig. 4 In vitro immune responses of MΦs on various nanostructures. (**a**) Schematic of the experimental design. (**b**) Representative CLSM images of immunofluorescence staining of MΦs that adhered to different PEEK specimens (green, M1 phenotype marker iNOS; red, M2 phenotype marker CD206; blue, DAPI). (**c**) Quantitative analysis of iNOS and CD206 expressions based on immunofluorescence staining. (**d**) Flow cytometric evaluation of CCR7 (M1 phenotype marker) and CD206 (M2 phenotype marker) expressions. (**e**) Relative mRNA expression levels of M1 macrophage-related genes (*iNOS* and *IL-1β*) and M2 macrophage-related genes (*CD206* and *IL-4*). (**f**) ELISA of pro-inflammatory cytokines (IL-1β and TNF-α) and anti-inflammatory cytokines (IL-4 and IL-10) secreted by MΦs cultured on different specimens. $n = 3$ independent experiments *per* group; $^{*}P < 0.05$ and $^{**}P < 0.01$

oxide synthase (iNOS) and C-C chemokine receptor type 7 (CCR7) are two critical markers of M1 MΦ [44, 45], whereas CD206 is highly expressed on the cell surface of M2 MΦs [46]. Double immunostaining of iNOS and CD206 was performed to examine the polarization status of MΦs attached to different PEEK groups. Expression of iNOS was significantly down-regulated in MΦs attached to the SP450 and SP550 specimens. Conversely, CD206 expression was up-regulated in MΦs attached to the SP450 and SP550 specimens (Fig. 4b-c).

Both CCR7 and CD206 were further used for flow cytometry to confirm the MΦ phenotypes on different PEEK specimens (Fig. 4d). The proportions of CCR7-expressing M1 MΦs on different PEEK nano/microstructures were: P (37.1%) > SP750 (22.1%) > SP550 (14.5%) > SP650 (13.7%) > SP450 (9.36%). The proportions of CD206-expressing M2 MΦs on different PEEK nano/microstructures were: P (11.4%) < SP750 (12.8%) < SP650 (16.0%) < SP550 (40.1%) < SP450 (42.0%). These results indicate that SP450 and SP550 specimens induced MΦs to switch to the M2 phenotype. Figure 4e summarizes the expression of M1 MΦ-related and M2 MΦ-related genes. Similar to protein expression, the SP450 specimens had the lowest expression levels of the M1 MΦ-related gene (*iNOS* and *IL-1β*) but the highest expression levels of M2 MΦ-related genes (*CD206* and *IL-4*). The secretion of MΦ-associated cytokines was evaluated using enzyme-linked immunosorbent assay (ELISA) (Fig. 4f). Compared with the other groups, MΦs that adhered to the SP450 specimens secreted the smallest amounts of pro-inflammatory cytokines (IL-1β and TNF-α) but the largest amounts of anti-inflammatory cytokines (IL-4 and IL-10). These results further demonstrated that SP450 was more effective in promoting MΦ polarization to the anti-inflammatory M2 phenotype, thereby shifting the inflammatory response toward a healing response.

Macrophages are recognized as a bridge between inflammation and disease resolution due to their phenotypic plasticity [47]. Nanostructured surfaces have demonstrated promising effects on reducing inflammation, cytokine production, and macrophage polarization [48]. For example, Zhu et al. showed that honeycomb-like TiO_2 structures on titanium substrates enhanced M2 polarization as the surface scale decreased [24]. Similarly, titanium nanotubular surfaces with smaller scales were associated with higher expression of M2 markers and anti-inflammatory cytokines [49, 50]. In the present study, irregular nano/microstructured surfaces with smaller scales significantly induced M2 phenotype polarization compared to larger-scale specimens, likely due to the prevalence of nanostructures on SP450. However, the underlying mechanisms and cellular events remain unclear.

Effect of mechanical cues from nano/microstructures on macrophage activation

Transcriptomic analysis of MΦs cultured on smooth PEEK and SP450 was performed to elucidate how PEEK nano/microstructures regulated the immune response of MΦs. Figure 5a shows the overall distribution of gene expression in each group, which was uniform. Compared with the smooth PEEK, SP450 up-regulated 226 differential expression genes (DEGs) and down-regulated 168 DEGs (Fig. 5b). Eight DEGs were selected for experimental validation through RT-qPCR. The result was consistent with the RNA sequencing results (Figure S3a-b). Figure 5c shows the hierarchical clustering heatmap. The DEGs between the two groups were analyzed using the Gene Ontology (GO) enrichment method. All gene enrichment terms were divided into three categories: biological process, cellular component, and molecular function. The top 15 enriched terms in each DEG category are shown in Fig. 5d. The genes enriched in the "biological process" category were predominantly innate immune response, immune system process, inflammatory response, cell adhesion, and regulation of transcription. In the "cellular component" category, DEGs were clustered in cytoplasm, plasma membrane, endoplasmic reticulum, and cytoplasmic vesicle. In the "molecular function" category, DEGs were significantly enriched in protein binding, calcium ion binding, adenosine triphosphate binding, and actin binding. It is worth noting that calcium ion binding and actin binding are both down-regulated (Fig. 5e). These results indicated that MΦ polarization may be closely related to the synthesis and transport of proteins, dynamic membrane binding, and cytoskeletal assembly.

The Kyoto Encyclopedia of Genes and Genomes (KEGG) analysis was performed to identify the signaling pathways involved in regulating MΦ phenotype switching and the immune microenvironment. Figure 5e shows representative up-regulated and down-regulated signaling pathways. In addition to cell adhesion molecules, cholesterol metabolism was up-regulated. Cholesterol crystals are considered potent drivers of inflammation in MΦs and have been shown to activate NLRP3 inflammasomes to promote IL-1β production [51, 52]. Previous studies reported that cellular cholesterol efflux may decrease intracellular lipid deposition and up-regulate M2 MΦ polarization [53, 54]. Therefore, nano/microstructures may mediate MΦ polarization by regulating cholesterol metabolism. In addition, Rap1, MAPK, IL-17, FoxO, cAMP, and Ras signaling pathways were down-regulated, which may be related to MΦ polarization [55–58].

The calcium signaling pathway was examined to understand how nano/microstructure regulates MΦ polarization. This pathway was significantly decreased in the KEGG analysis. Calcium influx has been reported to play

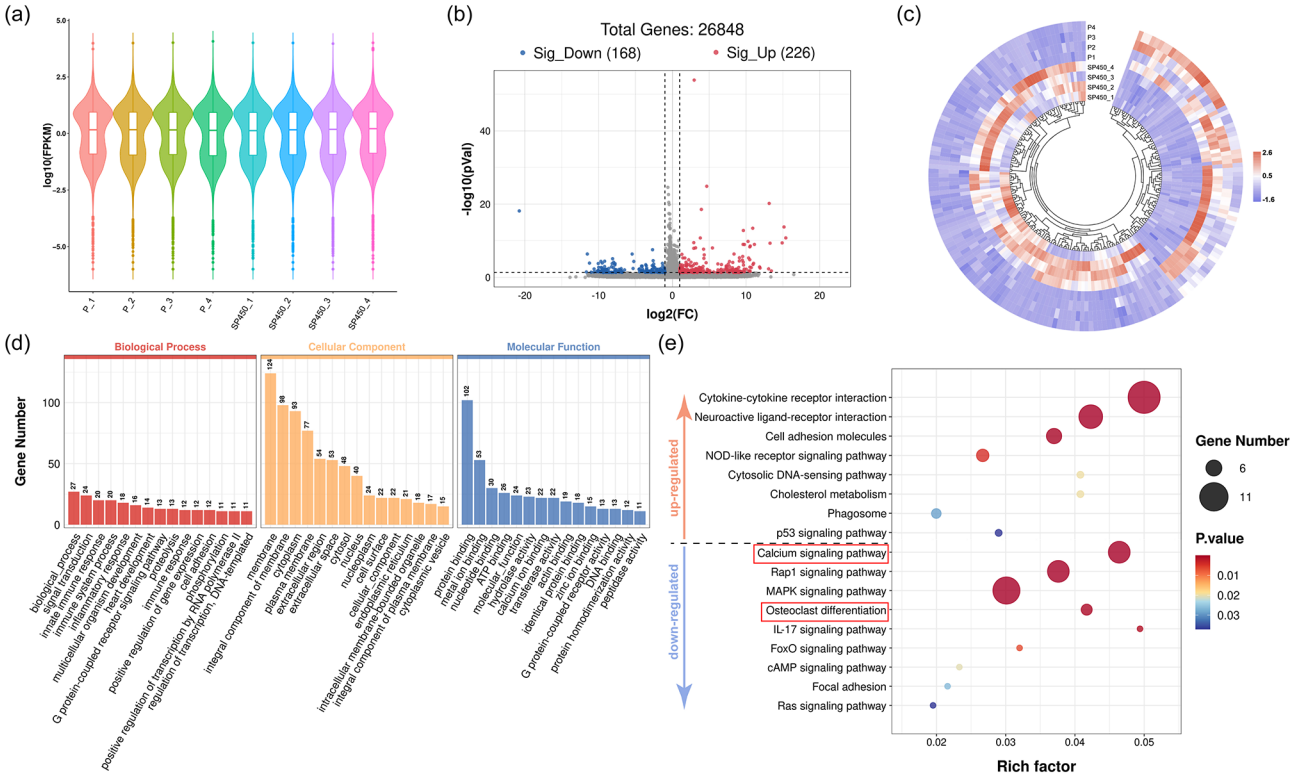

Fig. 5 Bioinformatic analysis of MΦ gene expression on smooth PEEK and SP450. (**a**) Violin diagram analysis. (**b**) Volcano plot of differential gene expressions. (**c**) Heatmap of distinct up-regulated and down-regulated genes of SP450 vs. P. (**d**) GO term enrichment analysis on biological process, cellular component, and molecular function of DEGs in SP450 vs. P. (**e**) KEGG pathway enrichment analysis of SP450 vs. P. $n = 4$ independent experiments *per* group

a critical role in promoting MΦ inflammatory activation [59]. The PIEZO1 channel is a novel type of mechanosensitive ion channel that regulates the influx of several cations, including Ca^{2+} [60]. Based on the DEG results, it was found that the mRNA expression of PIEZO1 was down-regulated in MΦs cultured with SP450, compared to the control P group (Figure S3a). This finding was consistent with the qPCR and western blot results (Figure S3b; Fig. 6a-b).

Yoda1, a specific agonist of Piezo1, significantly increased the protein expression of PIEZO1 in MΦs cultured with SP450 at a concentration of 20 μM (SP450Y), as shown by western blot analysis (Fig. 6a-b). Figure 6c shows that the MΦs cultured with SP450 had the lowest calcium content, which increased after the application of Yoda1. The Ca^{2+} influx mediated by PIEZO1 has been reported to promote actin polymerization [61]. The actin cytoskeleton, important in the modulation of MΦ inflammatory activation, was altered in response to the manipulation of PIEZO1 [44, 62]. Changes in actin resulting from PIEZO1 modulation were evaluated by staining with phalloidin, which binds to F-actin (Fig. 6d-e). Yoda1-mediated channel activation significantly enhanced F-actin fluorescent intensity compared to MΦs cultured with SP450. In addition, SP450 significantly reduced F-actin fluorescent intensity when compared with the P group. Polarization-related protein expression was also evaluated. Macrophages cultured with SP450 switched to the M1 phenotype after the application of Yoda1 (Fig. 6f-g). These results suggest that the expression of PIEZO1 was down-regulated by SP450, suppressing the inflammatory activation of MΦs. This suppression facilitates MΦ polarization toward the M2 phenotype. Previous studies have shown that PIEZO1 and actin interact positively to enhance inflammatory activation in MΦs. Mechanical cues, such as stiffness and surface topography, regulate macrophage polarization by modulating PIEZO1 activity [61, 63]. In vitro experiments conducted in this work revealed that the nanostructures on SP450 reduced PIEZO1-mediated calcium influx and inhibited actin polymerization, promoting macrophages toward the M2 phenotype (Fig. 6h). These findings suggest that biomaterial designs targeting PIEZO1 activity may offer a promising strategy to control tissue inflammation.

Effect of immune microenvironment generated by MΦs on osteogenic differentiation of osteoblasts

Recruitment of osteoblasts to the implant surfaces for new bone formation is influenced by the immune microenvironment [39]. Accordingly, the regulatory role of MΦ cytokines on osteogenic differentiation of osteoblasts was investigated using an indirect co-culture system (Fig. 7a).

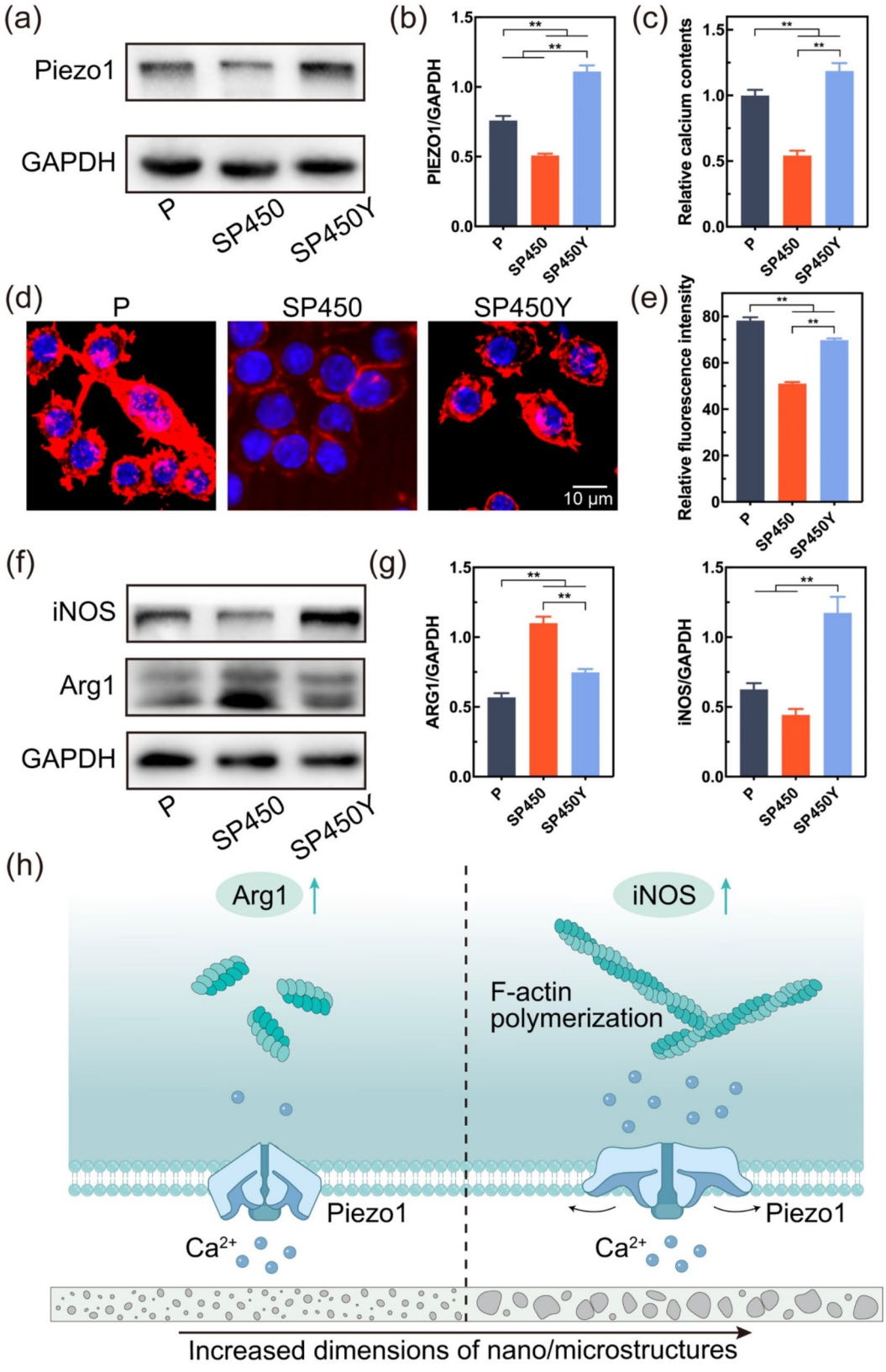

Fig. 6 (See legend on next page.)

(See figure on previous page.)

Fig. 6 SP450 down-regulates PIEZO1 to modulate MΦs activation in vitro. (**a**) Western blot images of PIEZO1 from MΦs cultured on different specimens or treated with 20 μM Yoda1. (**b**) Quantification of Piezo1 expression. (**c**) Quantitative analysis of calcium levels. (**d**) Representative fluorescent images of actin. (**e**) Quantification of actin. (**f**) Western blot images of ARG1 and iNOS. (**g**) Quantification of ARG1 and iNOS expression. (**h**) As the dimensions of nanostructures increased, Ca^{2+} influx mediated by the Piezo1 channel promoted actin polymerization. Positive regulation between actin and PIEZO1 enhanced inflammation through upregulation of inflammatory markers, such as iNOS. $n = 3$ independent experiments *per* group; $^{**}P < 0.01$

The MC3T3-E1 pre-osteoblasts were cultured in a conditioned medium that comprised a 1:1 ratio of MΦ supernatant and osteogenic medium. The sulfonated PEEK specimens exhibited slightly increased alkaline phosphatase activity on day 7 and day 14 (Fig. 7b). Alkaline phosphatase (ALP) activity in the SP450 group was markedly improved after supplementation of the osteogenic medium with MΦ supernatant (Fig. 7c). All specimens cultured in conditioned media demonstrated positive alkaline phosphatase staining results on day 7 and day 14 (Fig. 7d). There was significantly more insoluble blue-violet nitroblue tetrazolium-formazan in specimens derived from the SP450 group. The results of extracellular matrix mineralization by the differentiated osteoblasts were similar to the alkaline phosphatase activity (Fig. 7e, Figure S4a).

The expression of osteogenesis-related genes, including runt-related transcription factor 2 (*Runx2*), alkaline phosphatase (*Alp*), osteopontin (*Opn*), and osterix (*Ost*) was further examined with reverse transcriptase-quantitative polymerase chain reaction (RT-qPCR) (Fig. 7f). Cytokines released by M1 MΦs (TNF-α and IL-1β) inhibit osteogenic differentiation and activate osteoclastic bone resorption [15]. In the present study, MC3T3-E1 pre-osteoblasts exposed to the specimens derived from the SP650 and SP750 groups exhibited nondistinctive or even negative effects on inducing osteogenic differentiation. This is probably attributed to the influences of inflammatory cytokines secreted by M1 MΦs. In contrast, the expression of osteogenesis-related genes was significantly up-regulated in specimens from the SP450 and SP550 groups. This is probably attributed to anti-inflammatory IL-4 and IL-10 in the supernatant derived from pro-healing M2 MΦs in the SP450 and SP550 groups that promote osteogenic differentiation of the MC3T3-E1 pre-osteoblasts. Western blot analysis results of pre-osteoblasts cultivated for one week showed no significant difference in the expression levels of RUNX2, BMP2, and OCN between the P and SP750 groups. However, these expression levels were significantly lower than those shown in the SP450 group (Figure S4b-c). Based on this analysis, it is reasonable to conclude that SP450 enhanced osteogenesis and exhibited immunomodulatory activities in vitro.

To understand the potential underlying mechanisms by which MΦs influence osteogenic differentiation, gene expression in pre-osteoblasts cultured on SP450, with or without a conditioned medium, was analyzed using RNA sequencing. According to the DEGs clustering heatmap and volcano plot, 327 up-regulated genes and 159 down-regulated genes were identified in the group in which the conditioned medium was added, compared with the group without the conditioned medium (Figure S5a). GO analysis of the DEGs was performed using the OmicStudio platform. Differential gene expressions were identified in genes related to the cell membrane (e.g., calcium ion transport, sodium ion transport, transmembrane transport), the cytoskeleton (e.g., cytoskeleton organization, regulation of cell shape, structural constituents of cytoskeleton), transcription, cell adhesion, and cell proliferation (Figure S5b). The results indicated that the supernatant collected from MΦs cultured on SP450 explicitly altered transcriptional gene expression, cytoskeleton, and cellular morphology of the pre-osteoblasts.

KEGG analysis of DEGs was subsequently performed to identify the potential pathways activated by the MΦ supernatants (Figure S5d). In the "Metabolism" category, pyrimidine metabolism, steroid hormone biosynthesis, and purine metabolism were most enriched. Different signaling pathways were enriched in the "Environmental Information Processing" category. Those pathways included the calcium signaling pathway, TNF signaling pathway, ECM-receptor interaction, cell adhesion molecules, PI3K-AkT signaling pathway, cGMP-PKG signaling pathway, cAMP signaling pathway, TGF-beta signaling pathway, and Ras signaling pathway. Several genes associated with calcium signaling pathways, such as *Cacna1i*, *Grm1*, and *P2rx7*, were up-regulated in pre-osteoblasts cultured with conditioned medium. *Cacna1i* encodes the alpha subunit of T-type calcium channels, associated with osteogenic differentiation in bone marrow stem cells [64]. *Grm1* encodes metabotropic glutamate receptors, which are crucial for normal bone matrix production and skeletal development [65]. In addition, *P2rx7*, the receptor of SAA3 (up-regulated in macrophages from SP450, Figure S3a-b), plays a key role in osteogenesis [66]. These findings suggest that macrophages cultured on SP450 may mediate osteogenic differentiation of pre-osteoblasts through SAA3 secretion.

In vivo osseointegration and inflammatory responses of the implants

The in vitro results reported thus far suggested that SP450 induced polarization of MΦs into the M2 phenotype and that PEEK nano/microstructure has a scale-dependent effect on regulating MΦ polarization and

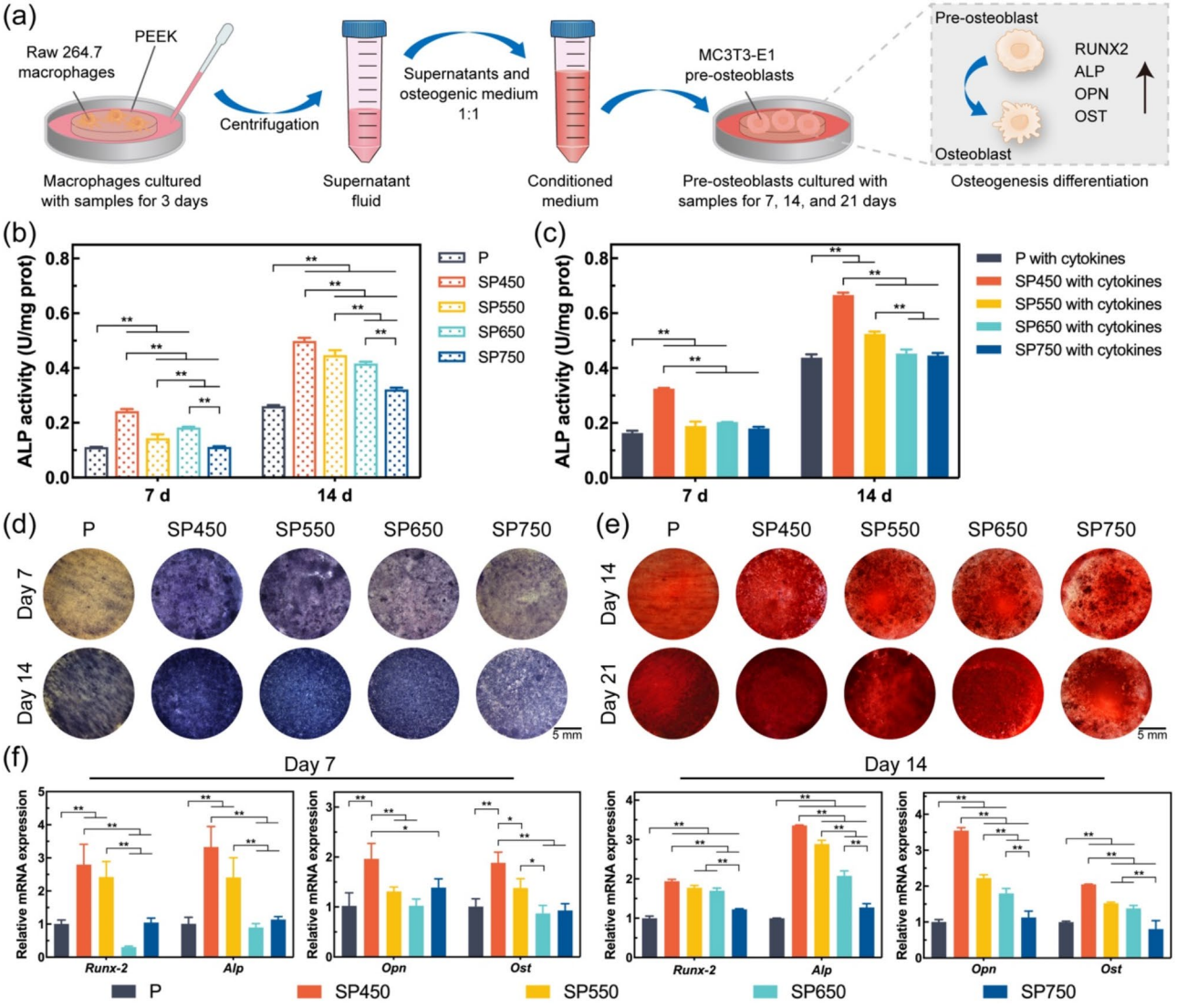

Fig. 7 In vitro osteogenic differentiation of pre-osteoblasts cultured on different PEEK specimens. (**a**) Schematic of osteogenic differentiation of pre-osteoblasts using conditioned medium derived from the supernatant of RAW 264.7 MΦs and osteogenic medium. (**b**) ALP activity of pre-osteoblasts cultured on different PEEK specimens without MΦ supernatants. (**c**) ALP activity of pre-osteoblasts cultured on different PEEK specimens in the presence of MΦ supernatants collected from corresponding PEEK specimens. (**d**) ALP staining of pre-osteoblasts cultured on different PEEK specimens with MΦ supernatants collected on day 7 and day 14. (**e**) Alizarin red S staining of pre-osteoblasts cultured on different PEEK specimens with MΦ supernatants collected on day 14 and day 21. (**f**) Gene expression of osteogenesis-related genes of pre-osteoblasts cultured on various PEEK specimens in the presence of MΦ supernatants. $n = 3$ independent experiments *per* group; $^{*}P < 0.05$ and $^{**}P < 0.01$

osteogenic differentiation. Hence, SP450 and SP750, the PEEK nano/microstructures with the minimum and maximum dimensions, were used to conduct in vivo validation experiments (Fig. 8a). Micro-computed tomography (micro-CT) of reconstructed 3D models showed significantly more new bone formation in the SP450 group after 4 weeks of implantation (Fig. 8b). This observation was verified with quantitative analysis of the micro-CT data (Fig. 8c). Values for bone volume fraction (BV/TV), trabecular number (Tb.N), and trabecular thickness (Tb.Th) values for SP450 were $0.2199 \pm 0.0032\%$, 1.7164 ± 0.0447 mm^{-1}, and 0.1343 ± 0.0122 mm, respectively. These values were significantly higher than those derived from the P and SP750 groups. The trabecular separation (Tb.Sp) value for SP450 was 0.4486 ± 0.0040 mm, lower than values derived from the other two groups. New bone formation at the bone-implant interfaces was visualized using methylene blue-acid fuchsin staining (Fig. 8d). The newly formed bone was in close contact with the SP450 implant, with a higher bone-implant contact ratio than the P and SP750 groups (Fig. 8e). In contrast, only a small amount of new bone was seen in defects coupled with the P and SP750 implants. The new bone in these two groups exhibited

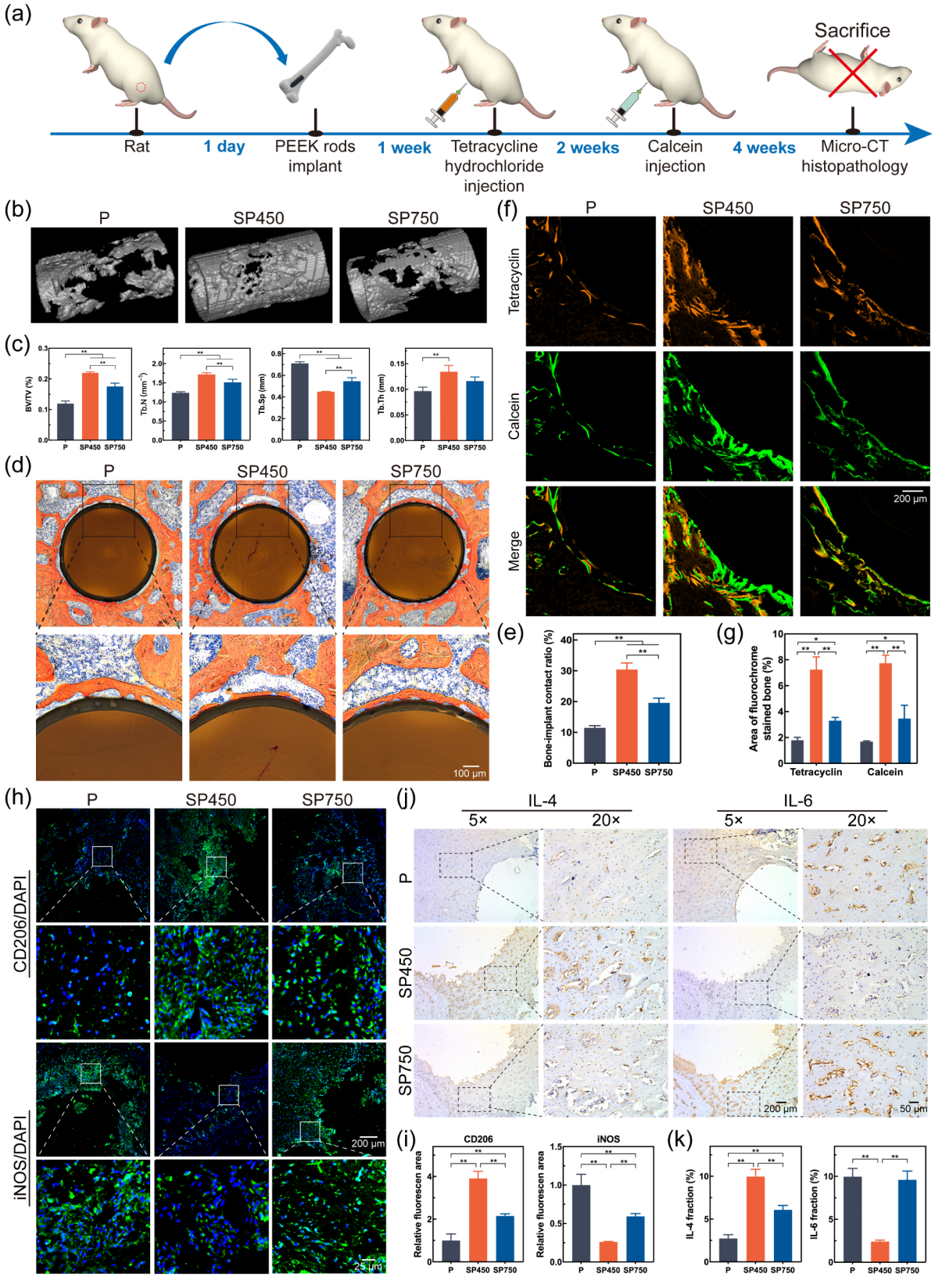

Fig. 8 (See legend on next page.)

(See figure on previous page.)

Fig. 8 In vivo osseointegration of PEEK implants prepared from P, SP450, and SP750. (**a**) Schematic of the placement of PEEK implants. (**b**) Micro-CT images of reconstructed 3D images of surrounding bones without implants. (**c**) Corresponding quantitative analysis of micro-CT results of BV/TV, Tb.N, Tb.Sp, and Tb.Th. (**d**) Histological images of methylene blue-acid fuchsin staining. (**e**) Bone-implant contact ratio. (**f**) Sequential fluorescent labeling. (**g**) Analysis of the fluorochrome-labeled new bone area. (**h**) Representative immunofluorescence staining of CD206 and iNOS. (**i**) Quantitative analysis of CD206 and iNOS positively-stained areas. (**j**) Representative immunohistochemical staining of IL-4 and IL-6. (**k**) Quantitative analysis of positively stained cells. $n = 3$ independent experiments *per* group; $^{*}P < 0.05$ and $^{**}P < 0.01$

point contact, and spaces between the newly formed bone and the implant surface were apparent. Fluorescent labeling confirmed the light microscopy staining results that implants prepared from SP450 had better new bone formation around the implants than those prepared from P or SP750 (Fig. 8f). Quantitatively, the percentages of the tetracycline hydrochloride-labeled area (orange) and calcein-labeled area (green) were significantly higher in the SP450 group than that of the P and SP750 groups (Fig. 8g). These results validated that SP450 effectively promoted osseointegration in vivo. Immunofluorescence staining of CD206 and iNOS (Fig. 8h) showed that the in vivo defects in the SP450 group had significantly a higher proportion of $CD206^{+}$ MΦs and a significantly lower proportion of $iNOS^{+}$ MΦs (Fig. 8i). Cytokine profiles in rat femur defects were subjected to histochemical staining (Fig. 8j). Significantly more IL-4 and less IL-6 were identified in the SP450 group (Fig. 8k). These results indicate that implantation of SP450 reduced inflammation response in the vicinity of the surgical defects and facilitated a more favorable immune microenvironment for osseointegration.

The immune system plays a pivotal role in early osseointegration at the implant-bone interface. Upon implant placement, acute inflammation is initiated, characterized by neutrophil recruitment and activation [20]. Monocytes are subsequently recruited and differentiate into macrophages, influenced by implant topographies [15]. PEEK implants with nanostructures enhance macrophage recruitment, reduce PIEZO1-mediated calcium influx, and inhibit actin polymerization, facilitating a switch from M1 to M2 macrophage phenotypes. This promotes osteogenesis by secreting anti-inflammatory cytokines like IL-4 and IL-10, thereby fostering an osteoimmune microenvironment conducive to early bone formation and implant stability.

SP450 inhibited osteoclastogenesis of MΦs in vitro and in vivo

The enriched KEGG pathways mentioned above included the osteoclast differentiation-related pathway, which was also down-regulated, in addition to the calcium signaling pathway (Fig. 5e). Macrophages are one of the precursors of osteoclasts and share the same myeloid cell lineage as osteoclasts [67]. The M1 MΦs have a higher potential for osteoclastic differentiation than M2-MΦs upon stimulation by receptor activator of nuclear factor κB ligand (RANKL) in vitro [68, 69]. Apart from fusing and differentiating into osteoclasts, MΦs may be involved in regulating osteoclast-mediated bone resorption. The M1 MΦs secrete pro-inflammatory TNF-α, IL-1β, and IL-6 to mediate the RANKL/RANK system to promote bone destruction by osteoclasts [70–72]. In contrast, IL-4, an anti-inflammatory cytokine, prevents osteoclastogenesis by inhibiting the activation of NF-κB and MAPK, reducing the expression of RANKL signaling [73]. IL-10 secreted by M2 MΦs inhibits osteoclastic activity by blocking the production of aforementioned pro-osteoclastic cytokines [74]. Hence, stimulating MΦs toward M2 polarization and suppressing osteoclastogenesis are of great importance in refraining excessive bone resorption during the early stage of bone remolding.

Bone resorption is the process in which mature osteoclasts decompose bone tissue by secreting catabolic factors. Cathepsin K (CTSK) and tartrate-resistant acid phosphatase (TRAP) are two principal proteases that participate in the degradation of type I collagen and resorption of bone matrix [75]. Osteoclast-related gene expression of MΦs cultured with smooth PEEK or SP450 was examined using qRT-PCR. As shown in Fig. 9a, gene expressions of CTSK and TRAP on SP450 were lower on MΦs cultured with smooth PEEK, which was consistent with the result of KEGG analysis. In addition, TRAP staining was performed on paraffin sections to detect osteoclast activity in vivo. Unlike the result derived from smooth PEEK, TRAP-positive areas were hardly seen in the SP450 specimens (Figure S6). These results suggest that the surface topography of SP450 may inhibit osteoclastogenesis. To understand how surface topography regulates MΦ behavior, the authors focused on DEGs related to osteoclastogenesis based on RNA-sequencing results. The mRNA expression of transforming growth factor-beta 2 (TGF-β2) was significantly down-regulated in the SP450 specimens. Several members of the TGF-β superfamily, such as TGF-β1, myostatin, and activin A, are important regulators of osteoclastogenesis. These factors regulate osteoclast differentiation through a mechanism dependent on RANKL/RANK interplay [76]. Nevertheless, the role of TGF-β2 in osteoclastogenesis is rarely mentioned in the literature, and the underlying mechanism has not been fully elucidated.

RAW264.7 MΦs differentiate into multinuclear mature osteoclasts upon stimulation by RANKL. To investigate the inhibitory effect of nano/microstructured surface

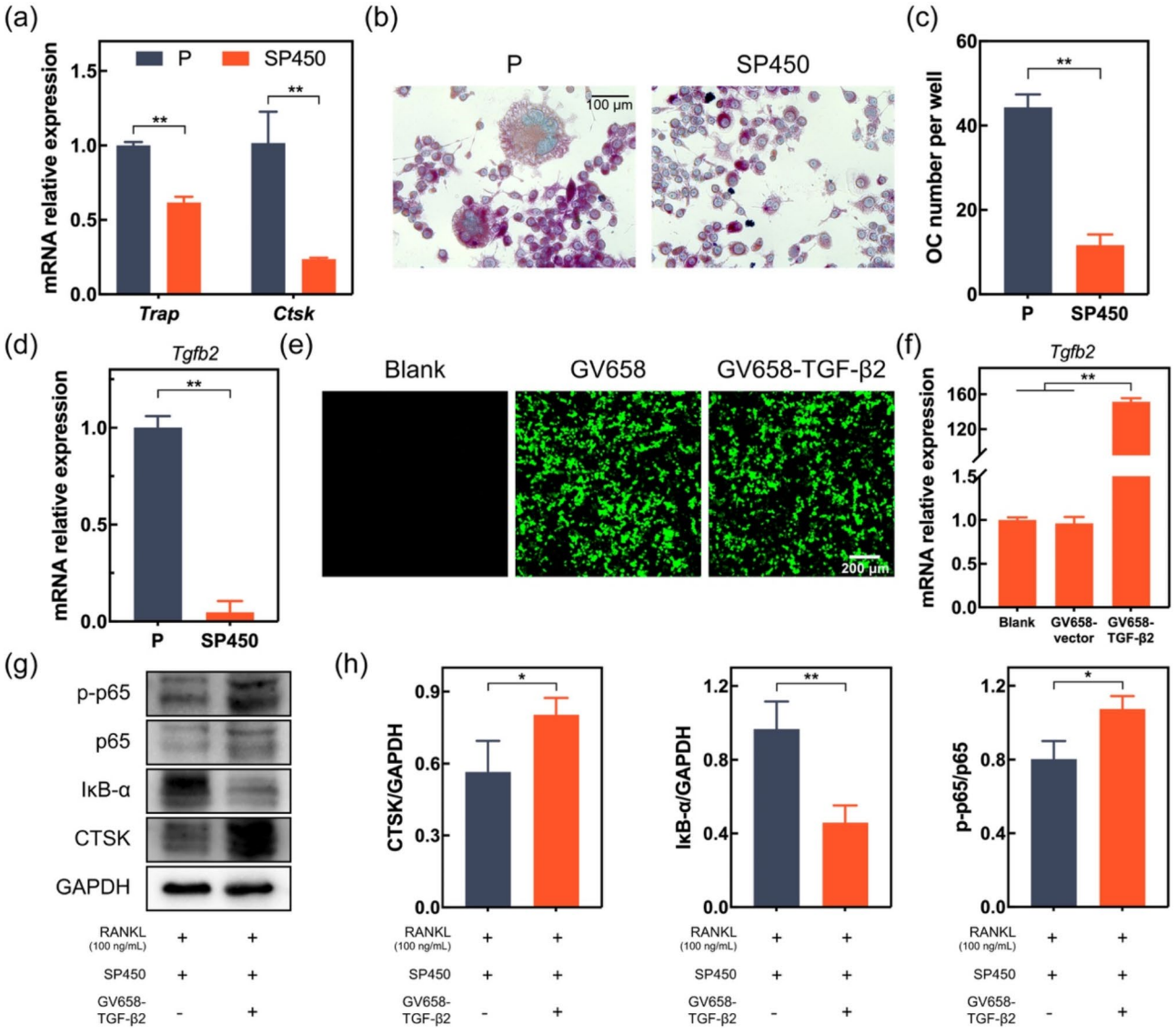

Fig. 9 SP450 inhibited osteoclastogenesis of MΦs in vitro. (**a**) Gene expression of TRAP and CTSK from MΦs cultured on P and SP450. (**b**) TRAP staining of MΦs cultured on P and SP450 treated with 100 ng/mL RANKL. (**c**) Quantification of TRAP-positive multinucleated cells. (**d**) Gene expression of TGF-β2 from MΦs cultured on P and SP450 treated with 100 ng/mL RANKL. (**e**) The fluorescent images of the blank group, GV658 group, and GV658-TGF-β2 group. (**f**) Transfection efficiency of TGF-β2 verified by qRT-PCR analysis. (**g**) Western blot images showing the levels of CTSK and NF-κB pathway proteins in MΦs cultured on SP450 treated with 100 ng/mL RANKL. (**h**) Quantification analysis of CTSK, IκBα, and p-p65/p65. $n = 3$ independent experiments *per* group; $^{*}P < 0.05$ and $^{**}P < 0.01$

topography on osteoclastic differentiation and the role of TGF-β2 in this process, MΦs were seeded on smooth PEEK or SP450 and incubated with RANKL (100 ng/mL). After 4 days of osteoclastic induction, TRAP staining showed the appearance of multinucleated and TRAP-positive osteoclasts on smooth PEEK, while there were only a few multinucleated cells on SP450 (Fig. 9b). Quantitative analysis of TRAP-stained cells further demonstrated that the number of multinucleated and TRAP-positive osteoclasts significantly decreased in the SP450 group (Fig. 9c). Likewise, gene expression of TGF-β2 was significantly downregulated in cells cultured on SP450 (Fig. 9d).

Osteoclastogenesis is characterized by a cascade of reactions involving multiple pathways and factors. Briefly, RANKL interacts with its receptor RANK to recruit TRAF6 and activate a cascade of intracellular signaling pathways [77]. Among these pathways, NF-κB is an important downstream transcription factor of the RANKL-RANK signaling pathway. The classic NF-κB pathway involves the degradation of IκBα, which allows nuclear translocation of the p65 subunit of NF-κB and NF-κB-dependent gene expression [78]. To further

explore the potential underlying mechanism of TGF-β2 in osteoclastogenesis, TGF-β2 was overexpressed to examine its effect on the NF-κB signaling pathway. GV658-TGF-β2 plasmids were transfected into MΦs, and TGF-β2 expression in positive cells was analyzed with green fluorescent protein imaging and qRT-PCR (Fig. 9e-f). Uninfected and infected MΦs were seeded on SP450, and MΦs were incubated with RANKL (100 ng/mL) for 4 days to induce osteoclastic differentiation. Overexpression of TGF-β2 increased the expression of CTSK. The result suggests that TGF-β2 overexpression increased osteoclastic differentiation of MΦs (Fig. 9g-h). Furthermore, TGF-β2 overexpression significantly increased RANKL-induced degradation of IκBα and the ratio of p-p65/p65 (Fig. 9g-h). These results suggest that the surface topography on SP450 suppressed osteoclastic differentiation of MΦs by inhibiting the NF-κB signaling pathway via down-regulation of TGF-β2. Nevertheless, further studies are required to examine the interaction between signaling pathways involved in this process.

Conclusions

A series of PEEK nano/microstructures with different dimensions were fabricated for the first time by controlling the agitation speed of sulfonation. The mechanism of how PEEK surface topography cues regulate MΦ polarization and the immune microenvironment was elucidated in the present study. Surface features on the PEEK, especially SP450, induced polarization of MΦs to the pro-healing M2 phenotype through down-regulation of pro-inflammation genes (iNOS, IL-1β) and cytokines (IL-1β, TNF-α), as well as up-regulation of anti-inflammation genes (CD206, IL-4) and cytokines (IL-4, IL-10). The surface structure of SP450 reduced PIEZO1-mediated calcium influx and inhibited actin polymerization, thereby facilitating MΦs toward M2 polarization. The optimal immune microenvironment created by SP450 relieved inflammatory response and promoted osteogenic differentiation of pre-osteoblasts in vitro. Moreover, SP450 suppressed osteoclastic differentiation of MΦs by inhibiting the NF-κB signaling pathway *via* down-regulation of TGF-β2. Consequently, the SP450 surface topography enhanced *de novo* bone formation and osseointegration. Results from the present study may provide a simple and efficient solution for improving osseointegration of PEEK-containing bone repair materials. Future studies involving more implant sites, extended time-points, and larger animal models are needed to further investigate the impact of SP450 surface characteristics on the immune response.

Methods

Samples preparation and characterization

Biomedical grade PEEK (Shaanxi Jukang Gaobo Medical Technology Co., LTD, China) was machined into 17 × 17 × 2 mm for in vitro testing. PEEK rods (Ø 1.8 × 4.0 mm) were used for animal experiments. All PEEK plates were mechanically polished with 600- to 2000-grit silicon carbide papers (Matador, Germany) and ultrasonically cleaned in acetone, ethanol, and deionized water in sequence. PEEK substrates were treated with concentrated sulfuric acid (95–98 wt%, MilliporeSigma, Burlington, MA, USA) for 30 s with different agitation speeds (450 rpm, 550 rpm, 650 rpm, and 750 rpm), and were named SP450, SP550, SP650, and SP750, respectively. The polished PEEK, the control group, was denoted as P. Magnetic stirring was used throughout the entire acid etching process at room temperature to obtain a uniform porous structure. After sulfonation, the SP450, SP550, SP650, and SP750 specimens were submerged in deionized water for 10 min. The sulfonated specimens were cleaned ultrasonically in acetone for 10 min. Hydrothermal treatment was then performed at 100 °C for 4 h to remove residual sulfuric acid. The PEEK specimens were dried at room temperature. All specimens were sterilized with autoclaving prior to use (121.3 °C, 103.4 kPa for 30 min).

The surface topography and structure of the prepared surfaces were inspected by FE-SEM (S-4800, Hitachi, Japan). EDS (SDD550, IXRF, USA) was used to analyze the elemental composition of the PEEK specimens. The roughness of the prepared surfaces was examined by AFM (Keysight 5500, Keysight Technologies, USA). Crystallinity was investigated using an XRD (XRD-7000, Shimadzu, Japan). FT-IR (FT-IR-8400 S, Shimadzu, Japan) was used to analyze the chemical groups of the specimens. Surface wettability was measured with a contact angle goniometer (Kruss, Germany), and deionized water was used as the test liquid. For protein absorption, the specimens were put into the 12-well plate. 500 μL 20 μg/mL FN was added into each well and incubated for 2 h at 37 °C. The total amount of adsorbed FN on different specimens was examined by BCA protein assay kit (CWBIO, China).

Cell culture

The murine-derived macrophage cell line RAW 264.7, and newborn mouse calvaria-derived MC3T3-E1 subclone 14 pre-osteoblasts were kindly provided by the Stem Cell Bank of the Chinese Academy of Sciences (Shanghai, China). The cells were cultured in Dulbecco's Modified Eagle Medium (DMEM) and *α*-MEM (Gibco, Thermo Fisher Scientific, Waltham, MA, USA), respectively, containing 1% penicillin-streptomycin (InCellGene LLC, Burlington, Ont, Canada) and 10% fetal bovine

serum (Gibco) at 37 °C in an incubator of 5% CO_2. Cell inoculation density was 1×10^4 cells/well unless otherwise specified. The MΦs were seeded onto PEEK specimens in 12-well plates. Supernatants were collected and centrifuged after 3 days of incubation. To investigate the influence of MΦs on osteogenesis, the supernatants collected from MΦs were mixed with osteogenic medium at a 1:1 ratio, as was designated the conditioned medium. The osteogenic medium consisted of a complete cell medium supplemented with 50 μg/mL ascorbic acid, 10 nM dexamethasone, and 10 mM β-glycerophosphate (Solarbio, China). The culture medium was replaced with the conditioned medium obtained from different PEEK surfaces on alternate days after the pre-osteoblasts had been seeded.

Cell behavior of MC3T3-E1 pre-osteoblasts cultured on different PEEK specimens

MC3T3-E1 adhesion

After 1 h, 2 h, and 4 h of culture, the specimens were washed with phosphate-buffered saline (PBS) and fixed with 4% paraformaldehyde. After staining with 4',6-diamidino-2-phenylindole (DAPI, RSKBIO, China) and washed with PBS, cell adhesion was examined using a fluorescence microscope.

Cytotoxicity and MC3T3-E1 proliferation

Cytotoxicity and cell proliferation were evaluated by a Calcein/PI live/dead viability/cytotoxicity assay kit (Beyotime, China) and a cell counting kit (CCK-8, Yeasen, China) according to the instructions, respectively. MC3T3-E1 cells were seeded on the specimens and cultured for 1 d, 3 d, and 7 d. For cytotoxicity assay, the specimens were rinsed once with PBS, and then 500 μL of working solution containing 1 μL/mL Calcein AM and PI mixture in PBS was dropped on each specimen surface. After 20 min of incubation in the dark, the specimens were observed by the CLSM. For the cell proliferation assay, 1 mL fresh medium (900 μL cell culture medium and 100 μL CCK-8 solution) was added to each well. Optical density (OD) was determined at 450 nm after incubating at 37 °C for 2 h.

MC3T3-E1 morphology

After 3 days of culture, the cells were fixed in 2.5% glutaraldehyde and dehydrated gradually in an ascending ethanol series (30%, 50%, 70%, 80%, 90%, and 100%). The morphology of MC3T3-E1 cells cultured on different PEEK specimens was observed with FE-SEM after drying and sputter coating with platinum.

Immune responses of MΦs cultured on different PEEK specimens

MΦ morphology

After 3 days of culture, the morphology of MΦs was observed by the SEM following the standard procedures detailed in *MC3T3-E1 morphology*.

MΦ adhesion

After 1 h, 2 h, and 4 h of culture, the initial adhesion behavior of MΦs on the specimens was visualized by DAPI staining as the previous description in *MC3T3-E1 adhesion*.

MΦ proliferation

After 1 d, 3 d, and 5 d of culture, the proliferation of MΦs on various PEEK specimens was evaluated as the previous description in *Cytotoxicity and MC3T3-E1 proliferation*.

Immunofluorescence staining

After 3 d of culture, the MΦs were fixed with 4% paraformaldehyde at room temperature, permeabilized with 0.2% Triton X-100 (G-Clone, China), and blocked with 10% goat serum (Incellgene). The MΦs were subsequently incubated with the primary antibodies of CD206 (mouse-anti-mouse, 60143-1-Ig, Proteintech, Rosemont, IL, USA) and iNOS (rabbit-anti-mouse, AF0199, Affinity Biosciences, China), with 1:500 dilution at 4 °C overnight. The specimens were incubated with the mixed secondary antibodies of Dylight 594 goat-anti-mouse IgG and Flour 488 goat-anti-rabbit IgG (both 1:500 dilution). Cell nuclei were stained with DAPI for observation with CLSM (TiE A1 Plus, Nikon, Japan).

Flow cytometry

Macrophages were seeded on different specimens at a density of 3×10^4 cells/well and incubated for 3 days. The MΦs were then blocked with 1% bovine serum albumin for 30 min at room temperature. The cells were incubated with Alexa Fluor 488-conjugated CCR7 and phycoerythrin-conjugated CD206 (Biolegend, USA) for 1 h at 37 °C. After washing twice with PBS, the cells were analyzed with a flow cytometer (Cytomics™ FC 500, Beckmancoulter, USA). 1×10^4 cells were analyzed in each test.

Gene expression of MΦs

Macrophages were seeded on different specimens at a density of 3×10^4 cells/well and incubated for 3 days. Total cellular RNA was extracted with Trizol reagent (Invitrogen, Thermo Fisher Scientific) following the manufacturer's instructions. Complementary DNA was synthesized with Hifair III 1st Strand cDNA Synthesis SuperMix (Yeasen, China). Gene expression of M1 markers IL-1β and iNOS, and M2 markers IL-4 and

CD206, was determined using a real-time PCR system (ABI7500, Applied Biosystems, Waltham, MA, USA) with 2×TSINGKE MASTER qPCR Mix (TsingKe Biological Technology, China). The primer sequences are listed in Table S1.

Enzyme-linked immunosorbent assay (ELISA)

Macrophages were seeded on different specimens at a density of 3×10^4 cells/well. After 3 days of culture, the culture media were collected and centrifuged. The supernatants were utilized for analyses. The concentrations of IL-1β, TNF-α, IL-4, and IL-10 were measured with ELISA kits (Cloud-Clone Corp., Katy, TX, USA), following the manufacturer's instructions.

Osteogenic differentiation of pre-osteoblasts in vitro

Alkaline phosphatase staining and activity

After 7 days and 14 days of osteogenic induction, the differentiated osteoblasts were fixed in 4% paraformaldehyde and washed thrice with PBS. The fixed cells were stained with the 5-bromo-4-chloro-3-indolyl-phosphate/nitroblue tetrazolium alkaline phosphatase (ALP) color development kit (Beyotime, China) according to the manufacturer's protocol. Optical images were taken with an inverted microscope (Lecia, Germany). For quantitative evaluation of ALP activity, the osteoblasts were lysed with 1% Triton X-100. Absorbance was recorded at 405 nm using an ALP assay kit (Beyotime, China). The ALP levels were normalized to the total intracellular protein content.

Alizarin red S staining

After 7 days and 14 days of osteogenic induction, the differentiated osteoblasts were fixed in 4% paraformaldehyde and washed thrice with PBS. The differentiated osteoblasts were incubated in Alizarin red S solution (Solarbio, China; pH = 4.2) for 10 min at room temperature. After washing with deionized water, the stained osteoblasts were examined with an inverted microscope (Lecia, Germany). For quantitative analysis, the specimens were dissolved in 1 mL of 10% cetylpyridinium chloride (Tianjin Guangfu Fine Chemical Research Institute, China) for 1 h. The eluate was transferred to a 96-well plate. Absorbance was recorded at 562 nm using a microplate reader (BioTek, Winooski, VT, USA).

Gene expression of differentiated osteoblasts

After 7 days and 14 days of osteogenic induction, the expression of osteogenesis-related genes *Runx2*, *Alp*, *Opn*, and *Ost* were measured by qRT-PCR. The primer sequences are listed in Table S1.

Protein expression of differentiated osteoblasts

After 7 days of osteogenic induction, the expression of osteogenesis-related proteins RUNX2, BMP2, and OCN were measured by western blot. Whole protein extraction was performed with RIPA buffer containing 100 mM protease and phosphatase inhibitor cocktail (Beyotime, China). The protein specimens were separated by 10% sodium dodecyl sulfate-polyacrylamide gel electrophoresis and transferred onto a polyvinylidine difluoride membrane (MilliporeSigma). The protein-containing membrane was blocked with protein-free rapid blocking buffer (EpiZyme Biotechnology, China) and blotted with primary antibodies at 4 °C overnight. The primary antibodies used were RUNX2 (Santa, sc-390351, 1:1000), BMP2 (Santa, sc-137087, 1:1000), OCN (Santa, sc-365797, 1:1000). This was followed by incubation with secondary antibodies (Affinity Biosciences, Cincinnati, OH, USA) at room temperature. Membrane bands were visualized using the ChemiDoc imaging system (Bio-Rad, Hercules, CA, USA) and analyzed using ImageJ software. Glyceraldehyde 3-phosphate dehydrogenase was used as endogenous control.

In vivo evaluation

Surgical procedure

Animal experiments were approved by the Laboratory Animal Ethical Inspection, School of Stomatology, Air Force Military Medical University (registration number: 2020-017), China. A rat femur implantation model was used to evaluate the immune response and osseointegration of the PEEK specimens in vivo. Eighteen male Sprague-Dawley rats (350–400 g, specific-pathogen-free grade) were randomly divided into three groups: P, SP450, and SP750. Surgical procedures were performed on both femurs of each rat. The rats were anesthetized with 30 mg/kg of 1.5 (w/v) pentobarbital for surgery. Cylindrical femoral defects (approximately 1.8 mm in diameter and 4 mm deep) were created in the distal femur above the medial femoral condyle under saline irrigation. Rod-shaped PEEK implants were then inserted into the bony crypts. The wounds were sutured in layers. To prevent infection, all rats were injected with 50 kU/kg penicillin for the first three days after operation.

Sequential fluorescent labeling

At 7 and 14 days post-surgery, three rats from each group were randomly selected for intraperitoneal injection with 25 mg/kg tetracycline hydrochloride (MilliporeSigma) and 20 mg/kg calcein (MilliporeSigma). Four weeks after surgery, all rats were euthanized using excess pentobarbital sodium. Femurs with implants were harvested and fixed in 4% paraformaldehyde for 48 h at 4 °C for subsequent use.

Micro-computed tomography

Each implant-containing femur was scanned with a micro-CT system (Inveon MM CT, SIEMENS, Germany). The scanning parameters were set at 80 kV and 500 μA, with 1000 ms of exposure time and a resolution ratio of 39 μm. A 2.0 mm diameter and 4.0 mm deep cylindrical region was taken as the volume of interest. The scanned images were 3D reconstructed using the analyzing software (Inveon Research Workplace 2.2). The reconstruction parameters used to evaluate new bone formation mainly consisted of new bone volume to total volume, trabecular thickness, trabecular number, and trabecular separation.

Histological and immunostaining evaluation

Six rats from each group were divided into two subgroups for analysis. One subgroup was used for undecalcified sections with sequential fluorescent labeling, while the other was used for decalcified sections with non-sequential fluorescent labeling. For undecalcified sections, femur condyle specimens with implants were embedded in methyl methacrylate and cut into 200-μm-thick serial sections. Each section was ground and polished to 50 μm thick for fluorescent double-labeling evaluation and methylene blue-acid fuchsin staining (Solarbio, China). For decalcified sections, the femur condyle samples were demineralized in 10% ethylenediamine tetra-acetic acid (pH 7.2) for 2 weeks at 37 °C. The solutions were changed every three days. Subsequently, the decalcified specimens were dehydrated using an ascending ethanol series, embedded in paraffin and prepared for paraffin sections with a thickness of 5 μm.

The paraffin sections were deparaffinized, rehydrated, and then treated with sodium citrate buffer (RSKBIO, China) to retrieve the antigen. For immunofluorescence staining, sections were blocked in 10% goat serum (Incellgene) and incubated with primary antibodies of iNOS (mouse-anti-rat, ab210823, 1:100 dilution, Abcam Plc, UK) and CD206 (rabbit-anti-rat, ab300621, 1:100 dilution, Abcam), overnight at 4 °C. The treated specimens were incubated with mixed secondary antibodies consisting of Flour 488 goat-anti-rabbit IgG (1:500 dilution) at room temperature. Cell nuclei were labeled with DAPI solution. Sections were sealed with a mounting medium for antifading (Incellgene, USA) and scanned by CLSM. For immunohistochemistry, hydrogen peroxide was used for blocking. The sections were incubated with primary antibodies consisting of IL-6 (rabbit-anti-rat, DF6087, 1:100 dilution, Affinity Biosciences) and IL-4 (rabbit-anti-rat, AF5142, 1:100 dilution, Affinity Biosciences) at 4 °C. The treated sections were then incubated with secondary antibodies (Zhongshan Golden Bridge Biotechnology, China) at 37 °C. The color was revealed with DAB chromogenic solution and counterstained with hematoxylin. Protein expression in cells was detected with an optical microscope and analyzed with the Image J software (National Institute of Health, Bethesda, MD, USA).

Transcriptome sequencing and data analysis

Transcriptome sequencing of MΦs

Macrophages were seeded on smooth PEEK and SP450 at a density of 3×10^4 cells/well. After culturing for 3 days, total RNA was isolated from the cells and purified with Trizol reagent (Invitrogen). The RNA amount and purity of each sample were quantified using NanoDrop ND-1000 (NanoDrop, Wilmington, DE, USA). RNA sequencing was performed with an illumine Novaseq™ 6000 (LC-Bio Technology Co., Ltd., China) following the manufacturer's recommended protocol. Bioinformatic analysis was performed using the OmicStudio tools (https://www.omicstudio.cn/tool).

Protein expression of MΦs

To investigate the mechanism of how topography directly affects macrophage phenotype, MΦs were seeded on smooth PEEK and SP450 at a density of 3×10^4 cells/well. MΦs in the third group were seeded on SP450 with 20 μM Yoda1 for 10 h. Western blot was used to analyze the protein expression of PIEZO1, ARG1, and iNOS. The protocol followed the standard procedures detailed in *Protein expression of differentiated osteoblasts*. The primary antibodies used were PIEZO1 (Affinity, DF12083, 1:1000), ARG1 (Affinity, DF6657, 1:1000), iNOS (Affinity, AF0199, 1:1000).

Ca^{2+} concentration

MΦs cultured on different specimens were lysed, and Ca^{2+} concentration was evaluated by a calcium colorimetric assay kit (Beyotime, China), according to the manufacturer's protocol.

Immunofluorescence staining

The MΦs were fixed with 4% paraformaldehyde at room temperature and permeabilized with 0.2% Triton X-100 (G-Clone, China). The MΦs were subsequently incubated with phalloidin-TRITC (Cohesion, CRG1039) with 1:200 dilution at room temperature. Cell nuclei were stained with DAPI for observation with CLSM (TiE A1 Plus, Nikon, Japan).

TGF-β2 overexpression and cell culture

In vitro TGF-β2 overexpression was achieved via transfection with mouse TGF-β2 overexpression plasmid (Genechem, China). The MΦs (30–50% confluence) were transfected with plasmid and lipofectamine 3000 reagents (Thermo Fisher Scientific), following the manufacturer's protocol. Twelve hours after the transfection, the original medium was replaced with fresh medium,

and the cells were incubated for 3 days. Forty-eight hours after transfection, the macrophages were examined with an inverted fluorescence microscope. The overexpression efficiency of TGF-β2 was measured with qRT-PCR.

The MΦs were seeded onto SP450 at a density of 3×10^4 cells/well. The cells were left untransfected or were transfected with GV658-TGF-β2 plasmid. At 6 h after transfection, the culture medium was changed to regular DMEM. 100 ng/mL RANKL (PeproTech, USA) was added to each group to induce differentiation of the MΦs into osteoclasts. The culture medium was refreshed every 2 days.

Trap staining

TRAP staining of MΦs was performed after 4 days of osteoclastogenesis induction. The cells were fixed with 4% paraformaldehyde and stained using a TRAP staining kit (Solarbio, China).

Gene expression of MΦs after osteoclastogenesis induction

Expression of osteoclastic-related genes *Ctsk*, *Trap*, *c-Fos*, and *Nfatc1* were measured by qRT-PCR. The primer sequences are listed in Table S1.

Protein expression of MΦs after osteoclastogenesis induction

Expression of osteoclastic-related proteins CTSK, p65, p-p65, and IκBα were measured by western blot, following the standard procedures detailed in *Protein expression of differentiated osteoblasts*. The primary antibodies used were CTSK (Abcam, ab19027, 1:1000), p65 (Cell Signaling Technology, Danvers, MA, USA, 8242, 1:1000), p-p65 (Cell Signaling Technology, 3033, 1:1000), IκBα (Cell Signaling Technology, 9242, 1:1000).

Transcriptome sequencing of differentiated osteoblasts

Osteoblasts were seeded on smooth PEEK or SP450 at a density of 1×10^4 cells/well. Osteoblasts incubated without the conditioned medium were used as the control. Osteoblasts incubated in MΦ conditioned medium were designated the experimental group. After culturing for 7 days, total RNA was isolated from the cells and purified with Trizol reagent (Invitrogen). RNA sequencing followed the procedures described in *Transcriptome sequencing of MΦs*.

Statistics

All experiments were performed at least three times. All data were presented as the mean ± standard deviation. Statistical analysis was performed with one-way or two-way analysis of variance, followed by Tukey post-hoc test, after ascertaining that the normality and homoscedasticity assumptions of the data sets were not violated. Statistical significance was considered at $^*P < 0.05$ and $^{**}P < 0.01$.

Supplementary Information

The online version contains supplementary material available at https://doi.org/10.1186/s12951-025-03272-7.

Supplementary Material 1

Acknowledgements
Not applicable.

Author contributions
Y.A and J.W. conceived and designed the experiments. Y.Z. and F.W. performed the experiments. L.L. analyzed the data. Y.Z. wrote the main manuscript text. Y.J. and F.R.T. provided advice and edited manuscript.

Funding
This work was financially supported by Foundation of National Clinical Research Center for Oral Diseases (No. LCA202204), Key Research and Development Program of Shaanxi (No. 2024GH-YBXM-19), Clinical New Technology Program of Air Force Medical University (No. LX2023-306), China Postdoctoral Science Foundation (No. 2019M653969), the Thousand Talents Plan of Shaanxi Province (to Jing Wang), Clinical Research Program of Air Force Medical University (No. 2024LC2423), the National Natural Science Foundation of China (No. 82101069), the Logistics Independent Research Project of PLA (No. C24LBJ032)，the Beijing Natural Science Foundation (No. 7242279), the Beijing Nova Program (No. 2023046), the Beijing Municipal Science & Technology Commission (No. Z221100007422130), and the Open Project of State Key Laboratory of Trauma and Chemical poisoning (No. SKLO202401).

Data availability
RNA-sequencing data supporting this study's findings have been deposited into the Gene Expression Omnibus repository (Accession number: GSE290857 and GSE290906). All data are available from the corresponding author on reasonable request.

Declarations

Ethics approval and consent to participate
All animal experiments were approved by The Laboratory Animal Ethical Inspection, School of Stomatology, the Fourth Military Medical University, and the registration number was 2020-017.

Consent for publication
Not applicable.

Competing interests
The authors declare no competing interests.

Received: 13 October 2024 / Accepted: 24 February 2025
Published online: 11 March 2025

References

1. Zheng Z, Liu P, Zhang X, Jingguo X, Yongjie W, Zou X, et al. Strategies to improve bioactive and antibacterial properties of polyetheretherketone (PEEK) for use as orthopedic implants. Mater Today Bio. 2022;16:100402.
2. Chen Z, Chen Y, Ding J, Yu L. Blending strategy to modify PEEK-based orthopedic implants. Compos Part B. 2022;250:110427.
3. Chen J, Cao G, Li Y, Li N, Du Z, Li X. Fabrication and biological evaluation of polyether ether ketone (PEEK)/bioceramic composites. Prog Nat Sci. 2022;32(3):334–9.
4. Zanjanijam AR, Major I, Lyons JG, Lafont U, Devine DM. Fused filament fabrication of PEEK: a review of process-structure-property relationships. Polym (Basel). 2020;12(8).
5. Gao A, Liao Q, Xie L, Wang G, Zhang W, Wu Y, et al. Tuning the surface immunomodulatory functions of polyetheretherketone for enhanced osseointegration. Biomaterials. 2020;230:119642.

6. Dong J, Wang W, Zhou W, Zhang S, Li M, Li N, et al. Immunomodulatory biomaterials for implant-associated infections: from conventional to advanced therapeutic strategies. Biomater Res. 2022;26(1):72.
7. Yuan B, Cheng Q, Zhao R, Zhu X, Yang X, Yang X, et al. Comparison of osteointegration property between PEKK and PEEK: effects of surface structure and chemistry. Biomaterials. 2018;170:116–26.
8. Dondani JR, Iyer J, Tran SD. Surface treatments of PEEK for osseointegration to bone. Biomolecules. 2023;13(3).
9. Xie L, Wang G, Wu Y, Liao Q, Mo S, Ren X, et al. Programmed surface on poly(aryl-ether-ether-ketone) initiating immune mediation and fulfilling bone regeneration sequentially. Innov (Camb). 2021;2(3):100148.
10. Liu X, Zhang H, Yan B, Yeung KWK, Liao Y, Ouyang L, et al. On-off phagocytosis and switchable macrophage activation stimulated with NIR for infected percutaneous tissue repair of polypyrrole-coated sulfonated PEEK. Adv Sci (Weinh). 2023;10(5):e2205048.
11. Wang H, Fu X, Shi J, Li L, Sun J, Zhang X, et al. Nutrient element decorated polyetheretherketone implants steer mitochondrial dynamics for boosted diabetic osseointegration. Adv Sci (Weinh). 2021;8(20):e2101778.
12. Zhao Y, Wong HM, Wang W, Li P, Xu Z, Chong EY, et al. Cytocompatibility, osseointegration, and bioactivity of three-dimensional porous and nanostructured network on polyetheretherketone. Biomaterials. 2013;34(37):9264–77.
13. Ouyang L, Zhao Y, Jin G, Lu T, Li J, Qiao Y, et al. Influence of sulfur content on bone formation and antibacterial ability of sulfonated PEEK. Biomaterials. 2016;83:115–26.
14. Li Y, Wang J, He D, GuoxiongZhu, Wu G, Chen L. Surface sulfonation and nitrification enhance the biological activity and osteogenesis of polyetheretherketone by forming an irregular nano-porous monolayer. J Mater Sci Mater Med. 2019;31(1):11.
15. Shirazi S, Ravindran S, Cooper LF. Topography-mediated immunomodulation in osseointegration; ally or enemy. Biomaterials. 2022;291:121903.
16. Yu YL, Wu JJ, Lin CC, Qin X, Tay FR, Miao L, et al. Elimination of methicillin-resistant Staphylococcus aureus biofilms on titanium implants via photothermally-triggered nitric oxide and immunotherapy for enhanced osseointegration. Mil Med Res. 2023;10(1):21.
17. Liu Z, Zhang J, Fu C, Ding J. Osteoimmunity-regulating biomaterials promote bone regeneration. Asian J Pharm Sci. 2023;18(1):100774.
18. Wu J, Shen P, Qin X, Yang Y, Lin C, Li X, et al. Self-supply of H2O2 and O2 by a composite nanogenerator for chemodynamic therapy/hypoxia improvement and rapid therapy of biofilm-infected wounds. Chem Eng J. 2023;459:141507.
19. Luo ML, Jiao Y, Gong WP, Li Y, Niu LN, Tay FR, et al. Macrophages enhance mesenchymal stem cell osteogenesis via down-regulation of reactive oxygen species. J Dent. 2020;94:103297.
20. Chen Z, Klein T, Murray RZ, Crawford R, Chang J, Wu C, et al. Osteoimmunomodulation for the development of advanced bone biomaterials. Mater Today. 2016;19(6):304–21.
21. Xiong Y, Mi BB, Lin Z, Hu YQ, Yu L, Zha KK, et al. The role of the immune microenvironment in bone, cartilage, and soft tissue regeneration: from mechanism to therapeutic opportunity. Mil Med Res. 2022;9(1):65.
22. Li J, Jiang X, Li H, Gelinsky M, Gu Z. Tailoring materials for modulation of macrophage fate. Adv Mater. 2021;33(12):e2004172.
23. Zhang Y, Chen S, Qin X, Guo A, Li K, Chen L, et al. A versatile chitosan-based hydrogel accelerates infected wound healing via bacterial elimination, antioxidation, immunoregulation, and angiogenesis. Adv Healthc Mater. 2024;13(19):e2400318.
24. Zhu Y, Liang H, Liu X, Wu J, Yang C, Wong TM et al. Regulation of macrophage polarization through surface topography design to facilitate implant-to-bone osteointegration. Sci Adv. 2021;7(14).
25. Pan H, Xie Y, Zhang Z, Li K, Hu D, Zheng X, et al. Immunomodulation effect of a hierarchical macropore/nanosurface on osteogenesis and angiogenesis. Biomed Mater. 2017;12(4):045006.
26. Tao B, Lan H, Zhou X, Lin C, Qin X, Wu M, et al. Regulation of TiO2 nanotubes on titanium implants to orchestrate osteo/angio-genesis and osteo-immunomodulation for boosted osseointegration. Mater Des. 2023;233:112268.
27. Wang W, Luo CJ, Huang J, Edirisinghe M. PEEK surface modification by fast ambient-temperature sulfonation for bone implant applications. J R Soc Interface. 2019;16(152):20180955.
28. Cheng Q, Yuan B, Chen X, Yang X, Lin H, Zhu X, et al. Regulation of surface micro/nano structure and composition of polyetheretherketone and their influence on the behavior of MC3T3-E1 pre-osteoblasts. J Mater Chem B. 2019;7(37):5713–24.
29. Ma R, Wang J, Li C, Ma K, Wei J, Yang P, et al. Effects of different sulfonation times and post-treatment methods on the characterization and cytocompatibility of sulfonated PEEK. J Biomater Appl. 2020;35(3):342–52.
30. Shi Y, Deng T, Peng Y, Qin Z, Ramalingam M, Pan Y, et al. Effect of surface modification of PEEK artificial phalanx by 3D printing on its biological activity. Coatings. 2023;13(2):400.
31. Wang M-L, Hsieh Y-M. Kinetic study of dichlorocyclopropanation of 4-vinyl-1-cyclohexene by a novel multisite phase transfer catalyst. J Mol Catal A-Chem. 2004;210(1–2):59–68.
32. Mendonca G, Mendonca DB, Aragao FJ, Cooper LF. Advancing dental implant surface technology–from micron- to nanotopography. Biomaterials. 2008;29(28):3822–35.
33. Chakrapani N, Wei B, Carrillo A, Ajayan PM, Kane RS. Capillarity-driven assembly of two-dimensional cellular carbon nanotube foams. Proc Natl Acad Sci U S A. 2004;101(12):4009–12.
34. Qi H, Shi M, Ni Y, Mo W, Zhang P, Jiang S, et al. Size-confined effects of nanostructures on fibronectin-induced macrophage inflammation on titanium implants. Adv Healthc Mater. 2021;10(20):e2100994.
35. Guo T, Oztug NAK, Han P, Ivanovski S, Gulati K. Influence of sterilization on the performance of anodized nanoporous titanium implants. Mater Sci Eng C Mater Biol Appl. 2021;130:112429.
36. Junkar I, Kulkarni M, Drasler B, Rugelj N, Mazare A, Flasker A, et al. Influence of various sterilization procedures on TiO2 nanotubes used for biomedical devices. Bioelectrochemistry. 2016;109:79–86.
37. Oh S, Brammer KS, Moon K-S, Bae J-M, Jin S. Influence of sterilization methods on cell behavior and functionality of osteoblasts cultured on TiO2 nanotubes. Mater Sci Eng C Mater Biol Appl. 2011;31(5):873–9.
38. Ling X, Jing X, Zhang C, Chen S, editors. Polyether ether ketone (PEEK) properties and its application status. IOP Conference Series: Earth and Environmental Science; 2020: IOP Publishing.
39. Zhao Y, Bai L, Zhang Y, Yao R, Sun Y, Hang R, et al. Type I collagen decorated nanoporous network on titanium implant surface promotes osseointegration through mediating immunomodulation, angiogenesis, and osteogenesis. Biomaterials. 2022;288:121684.
40. Lu WL, Wang N, Gao P, Li CY, Zhao HS, Zhang ZT. Effects of anodic titanium dioxide nanotubes of different diameters on macrophage secretion and expression of cytokines and chemokines. Cell Prolif. 2015;48(1):95–104.
41. Zhou R, Wei D, Cheng S, Feng W, Du Q, Yang H, et al. Structure, MC3T3-E1 cell response, and osseointegration of macroporous titanium implants covered by a bioactive microarc oxidation coating with microporous structure. ACS Appl Mater Interfaces. 2014;6(7):4797–811.
42. Tylek T, Blum C, Hrynevich A, Schlegelmilch K, Schilling T, Dalton PD, et al. Precisely defined fiber scaffolds with 40 Mum porosity induce elongation driven M2-like polarization of human macrophages. Biofabrication. 2020;12(2):025007.
43. Luu TU, Gott SC, Woo BW, Rao MP, Liu WF. Micro- and nanopatterned topographical cues for regulating macrophage cell shape and phenotype. ACS Appl Mater Interfaces. 2015;7(51):28665–72.
44. Jain N, Vogel V. Spatial confinement downsizes the inflammatory response of macrophages. Nat Mater. 2018;17(12):1134–44.
45. Dai H, Fan Q, Wang C. Recent applications of immunomodulatory biomaterials for disease immunotherapy. Explor (Beijing). 2022;2(6):20210157.
46. Zhang B, Zhang M, Sun Y, Li M, Han F, Wu C. Haversian bone-mimicking bioceramic scaffolds enhancing MSC-macrophage osteo-imunomodulation. Prog Nat Sci. 2021;31(6):883–90.
47. Garlet GP, Giannobile WV. Macrophages: the bridge between inflammation resolution and tissue repair?? J Dent Res. 2018;97(10):1079–81.
48. Kunrath MF, Diz FM, Magini R, Galarraga-Vinueza ME, Nanointeraction. The profound influence of nanostructured and nano-drug delivery biomedical implant surfaces on cell behavior. Adv Colloid Interface Sci. 2020;284:102265.
49. Wang J, Meng F, Song W, Jin J, Ma Q, Fei D, et al. Nanostructured titanium regulates osseointegration via influencing macrophage polarization in the osteogenic environment. Int J Nanomed. 2018;13:4029–43.
50. Ma QL, Zhao LZ, Liu RR, Jin BQ, Song W, Wang Y, et al. Improved implant osseointegration of a nanostructured titanium surface via mediation of macrophage polarization. Biomaterials. 2014;35(37):9853–67.
51. Yan J, Horng T. Lipid metabolism in regulation of macrophage functions. Trends Cell Biol. 2020;30(12):979–89.
52. Vassiliou E, Farias-Pereira R. Impact of lipid metabolism on macrophage polarization: implications for inflammation and tumor immunity. Int J Mol Sci. 2023;24(15).

53. Zhang Q, He J, Xu F, Huang X, Wang Y, Zhang W, et al. Supramolecular copolymer modified statin-loaded discoidal rHDLs for atherosclerotic anti-inflammatory therapy by cholesterol efflux and M2 macrophage polarization. Biomater Sci. 2021;9(18):6153–68.
54. Xu Y, Xu Y, Zhu Y, Sun H, Juguilon C, Li F, et al. Macrophage miR-34a is a key regulator of cholesterol efflux and atherosclerosis. Mol Ther. 2020;28(1):202–16.
55. Tang S, Chen P, Zhang H, Weng H, Fang Z, Chen C, et al. Comparison of curative effect of human umbilical cord-derived mesenchymal stem cells and their small extracellular vesicles in treating osteoarthritis. Int J Nanomed. 2021;16:8185–202.
56. Deng RH, Zou MZ, Zheng D, Peng SY, Liu W, Bai XF, et al. Nanoparticles from cuttlefish ink inhibit tumor growth by synergizing immunotherapy and photothermal therapy. ACS Nano. 2019;13(8):8618–29.
57. Lee J, Rodero MP, Patel J, Moi D, Mazzieri R, Khosrotehrani K. Interleukin-23 regulates interleukin-17 expression in wounds, and its inhibition accelerates diabetic wound healing through the alteration of macrophage polarization. FASEB J. 2018;32(4):2086–94.
58. Li Y, Tu Q, Xie D, Chen S, Gao K, Xu X, et al. Triamcinolone acetonide-loaded nanoparticles encapsulated by CD90(+) MCSs-derived microvesicles drive anti-inflammatory properties and promote cartilage regeneration after osteoarthritis. J Nanobiotechnol. 2022;20(1):150.
59. Mo J, Xu Y, Wang X, Wei W, Zhao J. Exploiting the protein Corona: coating of black phosphorus nanosheets enables macrophage polarization via calcium influx. Nanoscale. 2020;12(3):1742–8.
60. Coste B, Xiao B, Santos JS, Syeda R, Grandl J, Spencer KS, et al. Piezo proteins are pore-forming subunits of mechanically activated channels. Nature. 2012;483(7388):176–81.
61. Atcha H, Jairaman A, Holt JR, Meli VS, Nagalla RR, Veerasubramanian PK, et al. Mechanically activated ion channel Piezo1 modulates macrophage polarization and stiffness sensing. Nat Commun. 2021;12(1):3256.
62. Pergola C, Schubert K, Pace S, Ziereisen J, Nikels F, Scherer O, et al. Modulation of actin dynamics as potential macrophage subtype-targeting anti-tumour strategy. Sci Rep. 2017;7:41434.
63. Song JN, Liu K, Mei J, Wang L, Lin J, Du P, et al. Defined surface physicochemical cues inhibit M1 polarization of human macrophages using colloidal self-assembled patterns. ACS Appl Mater Interfaces. 2023;15(30):35832–46.
64. Kim MO, Jung H, Kim SC, Park JK, Seo YK. Electromagnetic fields and nanomagnetic particles increase the osteogenic differentiation of human bone marrow-derived mesenchymal stem cells. Int J Mol Med. 2015;35(1):153–60.
65. Musante I, Mattinzoli D, Otescu LA, Bossi S, Ikehata M, Gentili C, et al. Phenotypic characterization of Grm1(crv4) mice reveals a functional role for the type 1 metabotropic glutamate receptor in bone mineralization. Bone. 2017;94:114–23.
66. Agrawal A, Henriksen Z, Syberg S, Petersen S, Aslan D, Solgaard M, et al. P2X7Rs are involved in cell death, growth and cellular signaling in primary human osteoblasts. Bone. 2017;95:91–101.
67. Mata R, Yao Y, Cao W, Ding J, Zhou T, Zhai Z et al. The dynamic inflammatory tissue microenvironment: signality and disease therapy by biomaterials. Research (Wash D C). 2021;2021:4189516.
68. Liu H, Jiao Y, Forouzanfar T, Wu G, Guo R, Lin H. High-strength double-network silk fibroin based hydrogel loaded with icariin and BMSCs to inhibit osteoclasts and promote osteogenic differentiation to enhance bone repair. Biomater Adv. 2024;160:213856.
69. Liang B, Wang H, Wu D, Wang Z. Macrophage M1/M2 polarization dynamically adapts to changes in microenvironment and modulates alveolar bone remodeling after dental implantation. J Leukoc Biol. 2021;110(3):433–47.
70. Kitaura H, Marahleh A, Ohori F, Noguchi T, Shen WR, Qi J et al. Osteocyte-related cytokines regulate osteoclast formation and bone resorption. Int J Mol Sci. 2020;21(14).
71. Amarasekara DS, Yun H, Kim S, Lee N, Kim H, Rho J. Regulation of osteoclast differentiation by cytokine networks. Immune Netw. 2018;18(1):e8.
72. Wu Q, Zhou X, Huang D, Ji Y, Kang F. IL-6 enhances osteocyte-mediated osteoclastogenesis by promoting JAK2 and RANKL activity in vitro. Cell Physiol Biochem. 2017;41(4):1360–9.
73. Feng Y, Zhang R, Wang YR, Chen F, Luo Q, Cai C, et al. Inhibition of endoplasmic reticulum stress by 4-phenyl butyric acid presents therapeutic effects on periodontitis: experimental studies in vitro and in rats. Stem Cells Int. 2021;2021:6618943.
74. Wei H, Huang H, He H, Xiao Y, Chun L, Jin Z, et al. Pt-Se hybrid nanozymes with potent catalytic activities to scavenge ROS/RONS and regulate macrophage polarization for osteoarthritis therapy. Res (Wash D C). 2024;7:0310.
75. Li Z, Wang H, Zhang K, Yang B, Xie X, Yang Z, et al. Bisphosphonate-based hydrogel mediates biomimetic negative feedback regulation of osteoclastic activity to promote bone regeneration. Bioact Mater. 2022;13:9–22.
76. Fennen M, Pap T, Dankbar B. Smad-dependent mechanisms of inflammatory bone destruction. Arthritis Res Ther. 2016;18(1):279.
77. Jiao Y, Wang X, Chen JH. Biofabrication of AuNPs using coriandrum sativum leaf extract and their antioxidant, analgesic activity. Sci Total Environ. 2021;767:144914.
78. Lin L, Guo Z, He E, Long X, Wang D, Zhang Y, et al. SIRT2 regulates extracellular vesicle-mediated liver-bone communication. Nat Metab. 2023;5(5):821–41.

Publisher's note